Supplementary Information

for

Tuning the Quantum-Well Structure of Single-Crystal Layered Perovskite Heterostructures

Arundhati P. Deshmukh,[†,|] Yinan Chen,[§,|] Jamie L. Cleron,[†] Monique Tie,[ǂ] Jiajia Wen,[‖] Tony F. Heinz,[#,ǂ] Marina R. Filip,[§,*] Hemamala I. Karunadasa[†,‖,*]

[†]Department of Chemistry, Stanford University, Stanford, CA – 94305, USA. [§]Department of Physics, University of Oxford, Oxford OXI 3PU, UK. [ǂ]Stanford PULSE Institute, SLAC National Accelerator Laboratory, Menlo Park, CA – 94025, USA. [‖]Stanford Institute for Materials and Energy Sciences, SLAC National Accelerator Laboratory, Menlo Park, CA – 94025, USA. [#]Department of Applied Physics, Stanford University, Stanford, CA – 94305, USA.

[|]Equal contribution

**Corresponding authors*
Email: hemamala@stanford.edu; marina.filip@physics.ox.ac.uk

I. Experimental section

All syntheses were conducted under ambient conditions unless otherwise mentioned. All precursors were obtained from commercial vendors and used as obtained unless otherwise noted. Solvents were of reagent grade or higher purity. Reagents used: $PbCl_2$ (Sigma-Aldrich, 98%), trans-(4-aminomethyl)cyclohexane-carboxylic acid (Sigma-Aldrich, 97%), aminomethylcyclohexane (ACROS Organics, 97%), LiCl (Sigma-Aldrich, ≥99%), NaCl (Fisher Scientific, ≥99%). Abbreviations: AMCHC = *trans*-(4-aminomethyl)cyclohexanecarboxylic acid, AMC = (cyclohexylmethyl)ammonium, DME = dimethoxyether, DMF = dimethylformamide, PMMA = poly(methyl methacrylate).

Synthesis of $M_2(PbCl_2)(AMCHC)_2(PbCl_4)\cdot 2H_2O$ (1_M; M = Li or Na)

Stock solutions of 6M NaCl (saturated at room temperature) and LiCl were prepared in distilled water. Solid $PbCl_2$ (139 mg, 0.500 mmol) and AMCHC (78.6 mg, 0.500 mmol) were mixed with 2 mL of the aqueous NaCl or LiCl solutions and heated to 85 °C for 2 h (for **1_Na**) or 30 minutes (for **1_Li**). The solution was filtered while hot using a pre-heated glass pipet fitted with glass microfiber paper. The filtered solutions were allowed to slowly evaporate in capped shell vials with a needle inserted in the headspace. The synthesis with NaCl yielded colorless plate-like crystals (**1_Na**) whereas the synthesis with LiCl yielded thinner colorless flakes (**1_Li**). Solid **1_Li** is hygroscopic. The crystals were separated by vacuum filtration, washed with DME or Et_2O multiple times, and dried overnight under reduced pressure. Occasionally, the synthesis of **1_Na** led to a side phase with PXRD peaks at 8.49° and 11.36° (source Cu-K Phase-pure **1_Na** can be obtained by mixing $PbCl_2$ (510 mg, 1.83 mmol) and AMCHC (393 mg, 2.50 mmol) in 10 mL of NaCl solution and stirring vigorously at 62 ºC for 30 minutes, followed by hot filtration and slow evaporation (as described above). For slow evaporation, the sample was left on the same hotplate set to 30 ºC. After 14 h, the product was isolated by vacuum filtration and washed with ethanol. Elemental analysis: see Table S4 for ICP-MS analysis and Table S5 for C, H, N analysis.

Synthesis of $(AMC)_2PbCl_4$

Solid $PbCl_2$ (100 mg, 0.340 mmol) was added to 1 mL of 12M HCl and stirred until completely dissolved. Then, aminomethylcyclohexane (80.0 mg, 0.707 mmol) was added dropwise to the $PbCl_2$ solution to afford a colorless precipitate. The powder was filtered and washed with copious amounts of H_2O, followed by Et_2O, and dried under reduced pressure. Single crystals of $(AMC)_2PbCl_4$ were formed by dissolving the powder in DMF at 95 °C and recrystallizing by cooling slowly, at the rate of 3 °C/h. Colorless square plate-like crystals were obtained after recrystallization.

Crystal structure determination

Crystals were coated with Paratone-N oil, mounted on a Kapton® loop, transferred to a Bruker D8 Venture diffractometer equipped with a Photon II detector, and cooled under a stream of dry N_2. Frames were collected using ω and ψ scans with 17.012 keV synchrotron radiation (λ = 0.72880 Å) at Beamline 12.2.1, Advanced Light Source, LBNL for $(AMC)_2PbCl_4$ or with 17.445 keV Mo-Kα radiation (λ = 0.71073 Å) at the Stanford Nano Shared Facilities for **1_Na** and **1_Li**. Unit-cell parameters were refined against all data. Crystals did not show significant decay during data collection. Frames were integrated and corrected for Lorentz and polarization effects using SAINT 8.38a and were corrected for absorption effects using SADABS V2016/2.2 Space-group

assignments were based upon systematic absences, *E*-statistics, agreement factors for equivalent reflections, and successful refinement of the structure. The structures were solved by direct methods, expanded through successive difference Fourier maps using SHELXT, and refined against all data using the SHELXL-2014 software package as implemented in Olex2. Weighted *R* factors, R_w, and all goodness-of-fit indicators are based on F^2. Thermal displacement parameters for all non-hydrogen atoms were refined anisotropically. The positions of the hydrogen atoms were refined using AFIX 0 command in Olex2. Crystallographic data for all the structures reported here are shown in Table S3.

In the refinement of $(AMC)_2PbCl_4$, the highest-intensity unassigned *Q*-peak (located within the perovskite layer) has an intensity of ~4.5 e/Å^3. Bond lengths and bond angles between the unassigned *Q*-peaks match closely with those within the perovskite layer, which is probably a result of a small unresolved twin. Since the unresolved *Q*-peaks represent a perovskite layer with ~ 5% intensity, we decided not to model this.

Powder X-ray diffraction (PXRD)

PXRD measurements were performed on a Bruker D8 Advance diffractometer equipped with a Cu anode (Kα1 = 1.54060 Å, Kα2 = 1.54443 Å, Kα2/Kα1 = 0.5), fixed divergence slits with a nickel filter, and a LYNXEYE detector. The instrument was operated in a Bragg-Brentano geometry with a step size of 0.01° or 0.02° (2θ). Samples were manually ground in a mortar and pestle, dispersed in toluene, and drop cast on a glass cover slip. Simulated powder diffraction patterns were obtained from Mercury software (CSD).

Calculation of octahedral distortion parameters

In- and out-of-plane octahedral distortion parameters (D_{in}, D_{out} respectively) were obtained using a previously reported method (along with the MATLAB code reported therein) with minor modifications for the replacement of Br atoms with Cl.[1] Atomic positions for all the Pb and in-plane Cl atoms were treated as vectors using their Cartesian coordinates obtained from the CIFs. A plane passing through the co-ordinates of three non-colinear Pb atoms was defined. A Pb–Cl–Pb angle was calculated and its projections onto the plane of the Pb atoms and onto a vector perpendicular to this plane were obtained. This approach is also generalizable to the intergrowth layers of the reported structures herein as these layers contain 4 in-plane bridging Pb–Cl bonds.

Inductively coupled plasma – mass spectrometry (ICP-MS)

Powder samples were digested in 2% HNO_3 made in distilled water under ambient conditions. A series of dilutions were prepared using the same matrix in plastic Falcon tubes. All dilution factors were recorded by weight. ICP-MS measurements were carried out on a Thermo XSeries II operated by the Stanford Environmental Measurement Facility (EMF) under ambient conditions. All values are averages across three measurements.

C, H, N analysis

Samples were brought into a N_2-filled glovebox after drying overnight under reduced pressure, ground manually and sealed under N_2. C, H, N analysis was performed by Midwest Microlab (Indianapolis, IN). For **1_Li**, the measurement was performed under air free conditions due to its hygroscopic nature. For **1_Na**, the measurement was performed in air. All values are averages from two measurements.

Fourier transform-infrared (FT-IR) spectroscopy
FT-IR spectra were collected in the Attenuated Total Reflectance (ATR) mode using a Thermo-Fisher Nicolet 6700 spectrometer equipped with a Smart Orbit accessory with a germanium plate. The samples were in (undiluted) powder form manually ground in a mortar and pestle. For comparison, we also collected an IR spectrum of the free ligand (AMCHC) taken directly from the reagent bottle and manually ground. Due to the hygroscopic nature of **1_Li**, we initially observed a broad peak in the O–H region from the surface water. To avoid this, we performed FT-IR on powders dried under reduced pressure overnight and brought into a N_2-filled glovebox. The IR spectrum was collected under ambient conditions within ~5 minutes of exposure to air. All IR spectra were collected with a resolution of 4 cm^{-1} and averaged over 256 scans.

Thermogravimetric analysis (TGA)
TGA was performed on a Netzsch TG 209 F1 Libra Thermo-Microbalance with alumina pans at a heating rate of 1 °C/minute from 20 to 500 °C. Due to the hygroscopic nature of **1_Li**, powders were ground in a N_2-filled glovebox. The measurement was performed in air with an additional 70 °C equilibration step to remove any surface adsorbed water.

Diffuse reflectance spectroscopy
Diffuse reflectance was measured on a Shimadzu UV-2600 spectrometer equipped with an integrating sphere. $BaSO_4$ powder was used as the reflective medium. An approximately 2-3 mm thick layer of $BaSO_4$ was pressed on the integrating sphere sample holder, followed by a thin layer of the manually ground sample powder mixed with $BaSO_4$. Pressed $BaSO_4$ powders were used to obtain the background spectrum. Diffuse reflectance data were converted into pseudoabsorbance *F(R)* using the Kubelka-Munk function and normalized to the lowest-energy excitonic peak.[2]

Photoluminescence (PL) spectroscopy
Room-temperature PL and cryogenic PL (cryo-PL) were measured using a Horiba Jobin-Yvon Nanolog fluorimeter equipped with a 450-W xenon lamp and R928S detector. For room-temperature measurements, manually ground powders were deposited from toluene onto a black carbon tape and mounted on the sample holder. Cryo-PL measurements were done inside a liquid-nitrogen-cooled Janis ST-100 cryostat. Samples were manually ground and suspended in a viscous PMMA solution in toluene. This slurry was deposited on the cold finger sample holder covered with carbon tape and allowed to dry completely. The cryostat was evacuated to a pressure of ~ 10^{-4} Torr. The transfer line was inserted into the cryostat and the liquid nitrogen was kept at a steady minimal flow rate. A Lakeshore Autotune temperature controller equipped with a PID loop was used to set the temperature. Spectra were taken after equilibrating at the set temperature for at least 10 minutes. Appropriate longpass filters were used on the emission monochromator to filter out the scattered excitation for both room-temperature and cryo-PL measurements. All emission spectra were corrected for the Jacobian determinant while converting from wavelength to the energy scale.[3] Temperature-dependent PL intensities were calculated by integrating the area under the curves using the trapezoidal method. Full-width at half-maximum (FWHM) values were calculated by fitting the spectra to a Gaussian $y = a1.e^{\left(\frac{x-b1}{c1}\right)^2}$, where FWHM $2\sqrt{\ln 2}\cdot c1$.

Specific heat capacity
Heat capacity measurements were performed using a Physical Property Measurement System (PPMS) on a pressed pellet of powder samples weighing 1.9 mg and 2.9 mg for **1_Li** and **1_Na**,

respectively. The pellet was affixed to a sapphire platform using Apiezon-N grease. The contribution of the sample holder and grease was subtracted after measuring it separately.

Second harmonic generation (SHG)

SHG experiments were performed under ambient conditions on single crystals laid flat on Si/SiO_2 substrates. Since the plate-like heterostructures grow more rapidly along the directions of the inorganic layers, the crystallographic *a-b* plane is parallel to the substrate. Standard z-cut quartz (1 mm thick) was obtained from MTI Corp. A 1030 nm fundamental frequency laser (NKT One-Five Origami 10) was focused on the sample using a Nikon CFI Plan Fluor 20× objective at normal incidence. The generated SH (515 nm) is collected in epi-mode using the same objective. Power dependence measurements were performed using a neutral density filter wheel. Both the incident and reflected beams pass through a linear polarizer and half-waveplate mounted on a rotational stage allowing for 360° rotation of the polarization within the crystal plane. The SHG signal was detected using an EM CCD (Andor iXon Ultra) after passing through a 600 nm short-pass filter.

Photoluminescence (PL) lifetime

Powder samples for emission lifetime studies were placed in an NMR tube that was immersed into a quartz finger dewar that contained liquid N_2. Transient luminescence lifetime data were collected using an IBH Fluorocube instrument equipped with a Jobin Yvon detector and interfaced with a Horibia Fluorohub+ controller. A pulsed NanoLED N-330 (331 nm) excitation source was used for time-correlated single-photon counting (TCSPC) measurements. Data analysis was performed using a Horiba DAS6 software package. Lifetimes were obtained by fitting the decay curves to a biexponential equation, an amplitude-weighted average was used to calculate average lifetimes.

Computational Methods

We calculate the electronic band structure shown in Figure 4 of the main manuscript within density functional theory (DFT)[4] as implemented in the Quantum Espresso package (version 6.7).[5,6] We employ fully relativistic PBE norm-conserving pseudopotentials from the Pseudo Dojo repository,[7,8] with the following valence electron configurations: C $2s^2p^2$, N $2s^22p^3$, O $2s^22p^4$, Li $1s^22s^1$, Na $2s^22p^63s^1$, Pb $5d^{10}6s^2$ $6p^2$ and Cl $3s^23p^5$. We use a kinetic energy cutoff of 70 Ry and sample the Brillouin zone using a Γ centered 6×6×4 Monkhorst-Pack mesh, with reduced sampling along the direction perpendicular to the perovskite planes. In all calculations reported throughout this work, spin-orbit coupling is fully accounted for. Unless otherwise stated, calculations (including DFT and *GW*+BSE) are performed using atomistic models extracted directly from experiment, without performing structural optimization calculations. Additional structural relaxations using DFT with the PBE functional were carried out and discussed in the Supplementary Note 3.

We calculate quasiparticle eigenvalues within the *GW* approximation,[9] as implemented in the BerkeleyGW package[10] as $E_{nk}^{\mathrm{QP}} = \epsilon_{nk} + Z\left(\epsilon_{nk}\right)\left\langle n\,\mathrm{k}\left|\Sigma\left(\epsilon_{nk}\right) - V_{\mathrm{xc}}\right|n\,\mathrm{k}\right\rangle$, where ϵ_{nk} are the mean-field DFT-PBE eigenvalues, Σ is the electron self-energy operator, V_{xc} is the exchange-correlation potential, and Z is the quasiparticle renormalization factor expressed as $Z\left(\omega\right) = \left[1 - R\left(\partial\,\Sigma / \partial\,\omega\right)\right]^{-1}$.

In all cases, we perform one shot G_0W_0 calculations with a DFT-PBE starting point including spin-orbit coupling. Within the G_0W_0 approximation, the electronic self-energy is computed as the convolution of the screened Coulomb interaction W_0 and the single particle Green's function G_0, written as $\Sigma = i\,G_0\,W_0$. The single particle Green's function is calculated from the DFT

starting point as, $G_0(r,r';\omega)=\sum_{nk}\frac{\psi_{nk}(r)\psi^{*}_{nk}(r')}{\omega-\epsilon_{nk}-i\eta}$, where the summation runs over the occupied and unoccupied states indexed by *n* and the wave-vectors in the uniform grid sampling of the Brillouin zone, $\psi_{nk}(r)$ is the DFT mean field wave function with the corresponding energy eigenvalue ϵ_{nk}, and η is an infinitesimally small constant, positive for occupied states and negative for unoccupied states. The screened Coulomb interaction is given by the expression, $W_0(r,r';\omega)=\varepsilon^{-1}(r,r';\omega)v(r,r')$, where $v(r,r')=1/|r-r'|$ is the bare Coulomb potential and $\varepsilon(r,r';\omega)$ is the dielectric function. We model the frequency-dependence of the dielectric function via the Godby-Needs plasmon-pole model.[11]

We use a polarizability cutoff of 8 Ry and sum over a total of 940 bands and a *k* / *q*-point grid of 4×4×1 in all calculations. These parameters achieved converged quasiparticle corrections for the fundamental band gaps (Figure S1b), the gap between perovskite sublattice bands (Figure S1c), and the intergrowth sublattice bands at Γ (Figure S1d), within less than 0.1 eV for **1_Li**, and are in line with previous quasiparticle band gap calculations for previously reported lead-halide heterostructures.[12] The convergence of the high-frequency limit of the dielectric constant with respect to the dielectric cutoff and number of bands are plotted in Figure S1a. The convergence of quasiparticle band gaps and the gaps between the intergrowth and perovskite sublattices are shown in Table S1 and Figure S1 b-d.

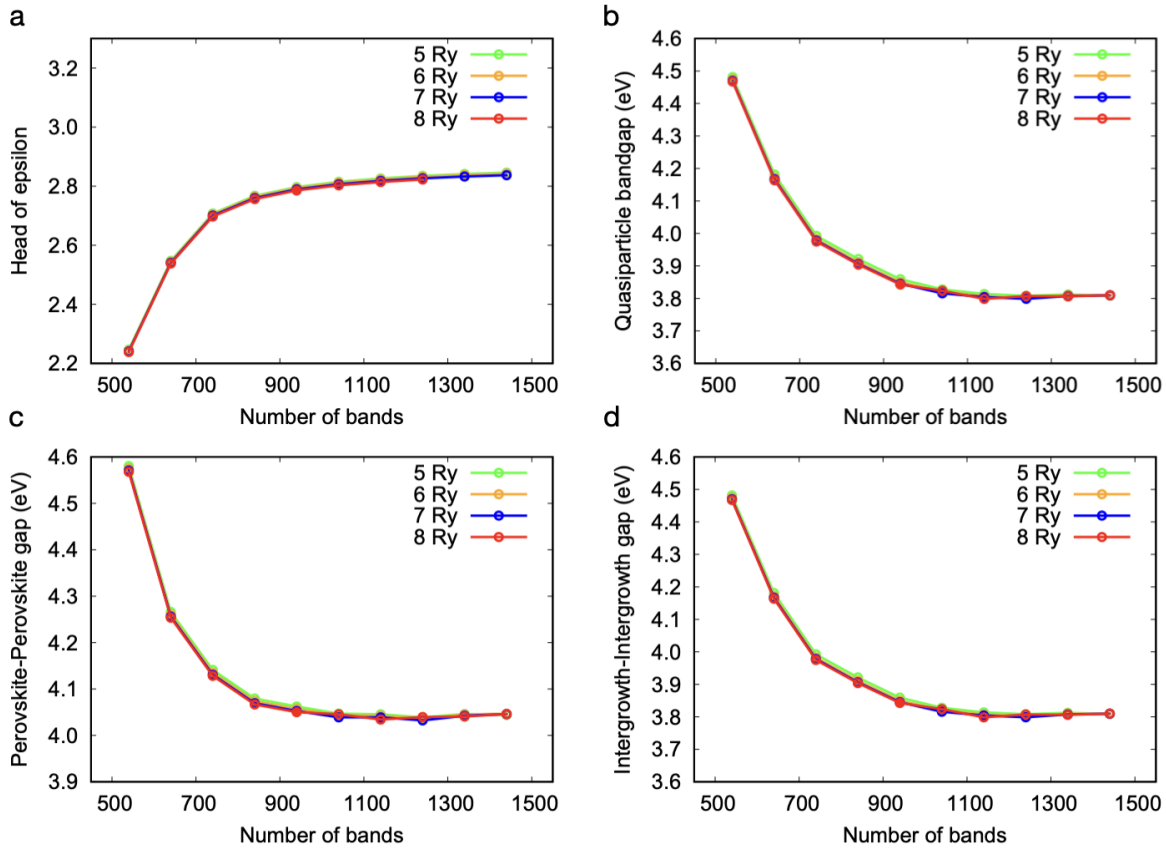

Figure S1. (a) Convergence of head of high frequency dielectric constants for **1_Li** with a 4 × 4 × 1 *k*-point grid. (b) Convergence of quasiparticle band gaps for **1_Li** with a 4 × 4 × 1 *k*-point grid. (c) Convergence of the gaps between quasiparticle eigenvalues from lowest conduction bands and highest valence bands from the perovskite layers of **1_Li** with a 4 × 4 × 1 *k*-point grid. (d) Convergence of the gaps between quasiparticle eigenvalues from the lowest conduction bands and highest valence bands from the intergrowth layers of **1_Li** with a 4 × 4 × 1 *k*-point grid.

We calculate the optical absorption spectra, including electron-hole interactions, by solving the Bethe-Salpeter equation (BSE) within the Tamm-Dancoff approximation,[13,14] as implemented in the BerkeleyGW package, $\left(E_{ck}^{\mathrm{QP}} - E_{vk}^{\mathrm{QP}}\right) A_{vck}^{S} + \sum_{v'c'k'} \left\langle vck \middle| K^{\mathrm{eh}} \middle| v'c'k' \right\rangle A_{v'c'k'}^{S} = \Omega^{S} A_{vck}^{S}$, where A_{vck}^{S} are the coefficients of the exciton wavefunction in the quasiparticle basis, Ω^{S} is the corresponding excitation energy of state, and K^{eh} is the electron-hole interaction kernel. The imaginary part of the dielectric function[10,13] is calculated as, $\varepsilon_2(\omega) = \frac{16\pi^2 e^2}{\omega^2} \sum_{S} \left| e \cdot \langle 0 | v | S \rangle \right|^2 \delta\left(\omega - \Omega^{S}\right)$, where we approximate the momentum operator, as discussed previously.[10] We construct the electron-hole kernel using 32 valence bands and 32 conduction bands in a coarse grid of 4×4×1 *k*-points and then interpolate it to a fine grid of 10×10×4 *k*-points. We use 20 valence bands and 20 conduction bands (including spin degeneracy) in the fine grid to calculate the absorption spectra. Based on convergence tests shown in Table S2, we estimate that exciton energies calculated within this setup are converged within less than 100 meV.

We calculate the two-particle exciton wave function using the eigenvectors A^S_{vck} of the BSE Hamiltonian, within the single-particle basis as $\Psi^S(r_e, r_h) = \sum_{cvk} A^S_{vck} \psi_{ck}(r_e) \psi^*_{vk}(r_h)$, where $r_{e(h)}$ corresponds to the position of the electron (hole), and $\psi_{c(v)k}$ are the single-particle (mean field) wave functions corresponding to unoccupied (occupied) states.

The exciton correlation function (ECF) $F(r)$ is defined as $F(r) = \int \left|\Psi_s(r_e = r_h + r, r_h)\right|^2 d r_h$,[15] which describes the probability of finding an electron and hole separated by a relative position vector, r, Furthermore, in order to describe the exciton localization across inorganic layers, we integrate the ECF along the in-plane directions of the supercell, to obtain the out-of-plane integrated and normalized ECF, $F_\perp(z) = \int_\Omega F(r)\, dxdy$, where z corresponds to the interlayer direction perpendicular to the layers whereas the x,y are in-plane directions.

For all excitonic states depicted, except the lowest-energy bright state of **1_Li,** we compute the integral in the ECF formalism as a discrete sum over r_h, sampled with a uniform grid in the primitive unit cell. In this expression, the real space wave function for each sample is r_h, computed using the plotxct.x utility of the BerkeleyGW package using a Fourier-transform real-space grid. The real space exciton wave function is computed in a 10 × 10 × 4 supercell to ensure wave function decay to less than 0.1% of the maximum value at the boundary. In the case of the lowest-energy bright state of **1_Li,** the procedure outlined above yielded an ECF that depicted spurious delocalization, which we attributed to convergence with respect to the hole position sampling in the out-of-plane direction. To test this, we randomly sample a total of 100 hole positions within the central primitive cell of the 10 × 10 × 4 supercell. The weights from the exciton wavefunction associated with each sampled hole are calculated using a Voronoi diagram of the sampling domain to account for non-uniform hole distributions.[16] This approach yielded a much improved ECF without spurious delocalization; consequently, the ECF depicted in Figure 8A of the main manuscript is computed using randomly sampled hole positions.

Table S1. Convergence of quasiparticle band gaps, the gaps between quasiparticle eigenvalues from lowest conduction bands and highest valence bands from intergrowth layer and lowest conduction bands and highest valence bands from the perovskite layer for **1_Li** with respect to *k*-point grid with 8 Ry dielectric cutoff energy and 940 empty bands. Bold parameters and gaps correspond to the final converged set of parameters.

***k*-point grid**	**VBM – CBM (eV)**	**Perovskite (eV)**	**Intergrowth (eV)**
4 × 4 × 1	**3.099**	**4.057**	**3.850**
4 × 4 × 2	3.114	4.075	3.863
6 × 6 × 1	3.096	4.057	3.848
8 × 8 × 1	3.098	4.059	3.850

Table S2. Convergence of excitation energy for lowest dark, first bright excitons and the energy difference for the two bright peaks in **1_Li** with respect to *k*-point grid and number of bands. Bold parameters and gaps correspond to the final converged set of parameters.

Coarse grid	Fine grid	Number of bands	Dark (eV)	Bright 1 (eV)	ΔE (eV)
4 ×4 × 1	8 × 8 × 4	20 + 20	2.708	3.078	0.262
4 × 4 × 1	10 × 10 × 1	20 + 20	2.701	3.039	0.242
4 × 4 × 1	**10 × 10 × 4**	**20 + 20**	**2.710**	**3.064**	**0.238**
4 × 4 × 1	12 × 12 × 1	20 + 20	2.716	3.043	0.263
4 × 4 × 1	10 × 10 × 4	12 + 12	2.710	3.074	0.239
4 × 4 × 1	10 × 10 × 4	16 + 16	2.710	3.066	0.244
4 × 4 × 1	10 × 10 × 4	24 + 24	2.710	3.059	0.240
4 × 4 × 2	10 × 10 × 4	20 + 20	2.767	2.990	0.241

II. Supporting data

Table S3. Crystallographic data table for **1_Na**, **1_Li**, and $(AMC)_2PbCl_4$.

Compound	**1_Na**	**1_Li**	$(AMC)_2PbCl_4$
Empirical formula	$C_{16}H_{34}Cl_6N_2Na_2O_6Pb_2$	$C_{16}H_{34}Cl_6Li_2N_2O_6Pb_2$	$C_{14}H_{32}Cl_4N_2Pb$
Formula weight	1024.31	991.41	577.40
Temperature/K	100	296.15	100
Crystal system	monoclinic	monoclinic	orthorhombic
Space group	*C*2	*C*2	$Cmc2_1$
a/Å	8.1801(4)	8.0506(3)	33.297(3)
b/Å	7.7431(3)	7.8685(3)	7.9305(6)
c/Å	23.3733(10)	23.6145(8)	7.7827(6)
α/°	90	90	90
β/°	92.431(2)	90.8850(10)	90
γ/°	90	90	90
Volume/Å^3	1479.12(11)	1495.71(9)	2055.1(3)
Z	2	2	4
ρ_{calc}/gcm^{-3}	2.300	2.201	1.866
μ/mm^{-1}	11.886	11.809	9.234
F(000)	961.0	928.0	1120.0
Crystal size/mm^3	0.15 × 0.075 × 0.02	0.2 × 0.075 × 0.02	0.05 × 0.03 × 0.02
Radiation	MoKα (λ = 0.71073)	MoKα (λ = 0.71073)	Synchrotron (λ = 0.7288)
2Θ range for data collection/°	5.234 to 56.604	5.176 to 56.576	5.018 to 54.312
Index ranges	$-10 \le h \le 10$, $-10 \le k \le 10$, $-31 \le l \le 31$	$-10 \le h \le 10$, $-10 \le k \le 10$, $-31 \le l \le 31$	$-41 \le h \le 41$, $-9 \le k \le 9$, $-9 \le l \le 9$
Reflections collected	19836	26867	18149
Independent reflections	19836 [R_{int} = ?,[b] R_{sigma} = 0.0637]	3707 [R_{int} = 0.0549, R_{sigma} = 0.0306]	2132 [R_{int} = 0.0490, R_{sigma} = 0.0296]
Data/restraints/parameters	19836/1/156	3707/1/188	2132/1/103
Goodness-of-fit on F^2	1.061	1.117	1.051
Final *R* indexes [I>=2σ (I)][a]	R_1 = 0.0343, wR_2 = 0.0853	R_1 = 0.0176, wR_2 = 0.0424	R_1 = 0.0245, wR_2 = 0.0613
Final *R* indexes [all data][a]	R_1 = 0.0350, wR_2 = 0.0859	R_1 = 0.0178, wR_2 = 0.0425	R_1 = 0.0255, wR_2 = 0.0618
Largest diff. peak/hole / e Å^{-3}	0.99/−1.31	0.59/−0.61	4.56/−0.70
Flack parameter	0.000(7)	0.003(5)	0.144(10)

[a] $R_1 = \sum \left| |F_o| - |F_c| \right| / \sum F_o$, $w R_2 = \left[\sum_w \left(F_o^2 - F_c^2 \right)^2 / \sum \left(F_o^2 \right)^2 \right]^{\frac{1}{2}}$

[b] R_{int} is undefined since **1_Na** was refined as a non-merohedral twin.

Table S4. Elemental analysis for Pb, Na, and Li content (in wt.%) in **1_Na** and **1_Li** obtained from inductively coupled plasma – mass spectrometry (ICP-MS).

Element	**1_Li**		**1_Na**	
	Expected (wt.%)	Obtained (wt.%)	Expected (wt.%)	Obtained (wt.%)
Pb	41.8	41.4	40.5	37.3
Li	1.4	1.9	-	-
Na	-	-	4.5	5.4

Table S5. Elemental analysis for carbon, hydrogen, and nitrogen content (in wt.%) for **1_Na** and **1_Li**.

Element	**1_Li**		**1_Na**	
	Expected (wt.%)	Obtained (wt.%)	Expected (wt.%)	Obtained (wt.%)
C	19.38	19.30	18.78	18.45
H	3.46	3.46	3.35	3.05
N	2.82	2.83	2.74	2.63

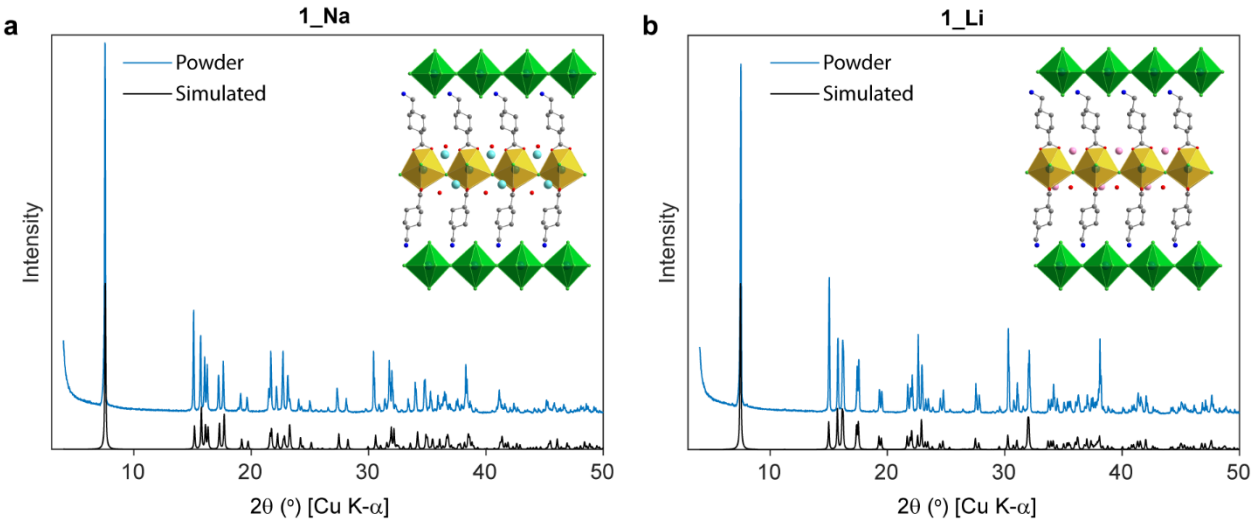

Figure S2. Experimental (blue) and simulated (black) powder X-ray diffraction (PXRD) patterns for a) **1_Na** and b) **1_Li**. Insets show the structure of the respective heterostructure. Perovskite and intergrowth layer Pb-centered polyhedra are shaded green and yellow, respectively. Atom colors: Pb: teal; Cl: green; Na: cyan, O: red; N: blue; C: grey; Li: pink. Hydrogen and disordered atoms are omitted for clarity.

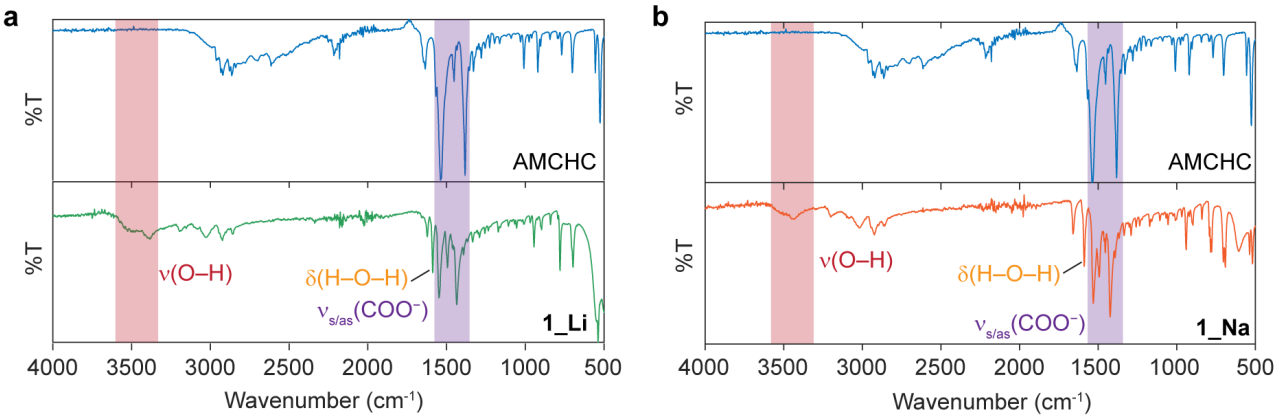

Figure S3. Attenuated total reflectance (ATR) Fourier transform-infrared (FT-IR) spectrum of the as-obtained ligand AMCHC (blue) compared to the spectrum of the heterostructures a) **1_Li** (green) and b) **1_Na** (orange). The difference between the symmetric and symmetric COO- stretching modes (highlighted in purple) is reduced in the heterostructures compared to that of the zwitterionic ligand, confirming bidentate binding to Pb in the heterostructures. The O–H stretch (highlighted in red) and H–O–H bend (marked in yellow) from the crystallographic water is also shown.

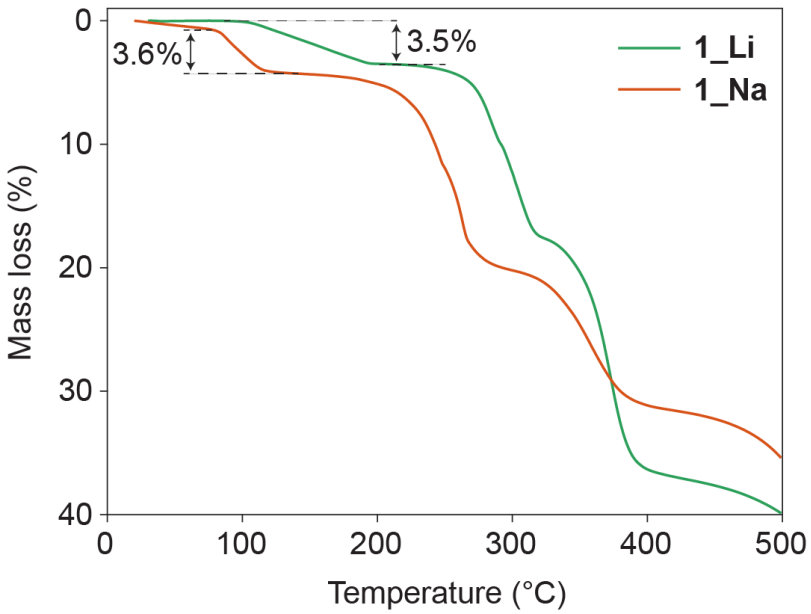

Figure S4. Thermogravimetric analysis of **1_Na** (orange) and **1_Li** (green) showing the initial mass loss of 3.6% at 70 – 130 °C for **1_Na** and 3.5% at 100 – 200 °C for **1_Li**, which match the expected mass loss for two H_2O molecules per formula unit: 3.5% and 3.6% for **1_Na** and **1_Li**, respectively. Water loss occurs at higher temperature in **1_Li** likely due to the stronger Li–O bond.

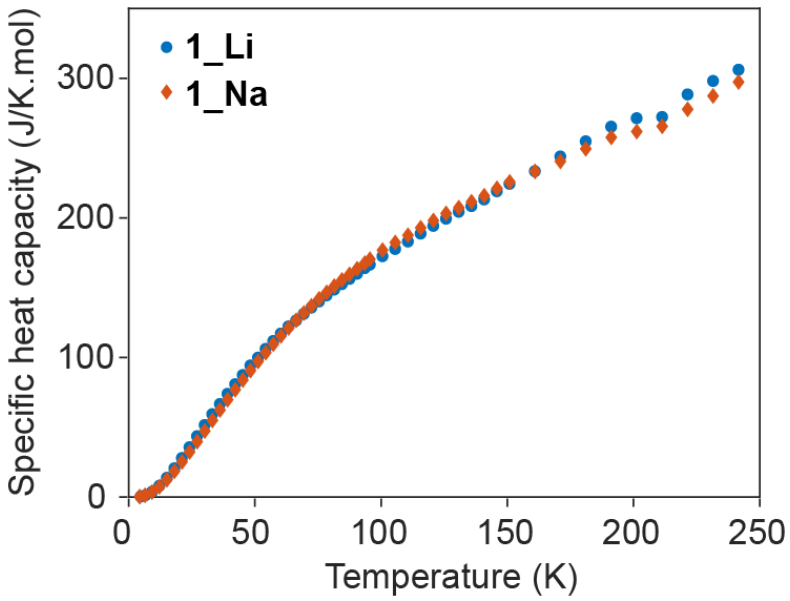

Figure S5. Specific heat capacity from 4 K to 300 K for **1_Li** (blue circles) and **1_Na** (red diamonds) in pressed powder pellet form. The lack of any sharp features indicates the absence of a phase transition in this range.

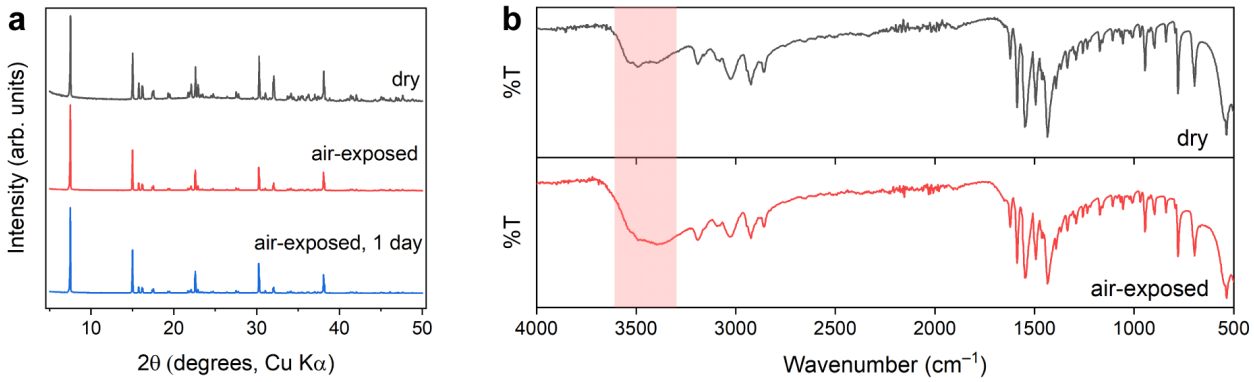

Figure S6. a) PXRD patterns and b) ATR FT-IR spectra of dry and air-exposed samples of **1_Li**. "Dry" samples were pulverized in a N_2-filled glovebox then briefly dried under reduced pressure, whereas "air-exposed" samples were pulverized in ambient air, followed by 1–2 h (red) or 1 day (blue) of air exposure. The IR spectrum of the air-exposed sample of **1_Li** shows a broad peak in the O–H stretch region due to adsorbed water, with no evidence of bulk degradation or loss of crystallinity after a day of air exposure. The FT-IR spectrum of the dry sample was collected under a stream of flowing N_2. PXRD patterns were obtained in ambient conditions.

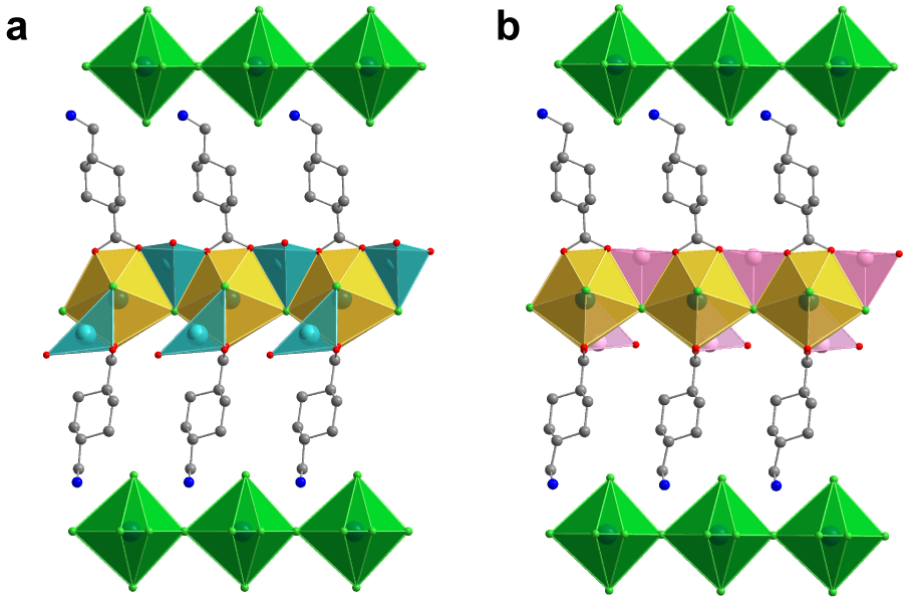

Figure S7. Single-crystal X-ray diffraction structures of a) **1_Na** and b) **1_Li** depicting the distorted trigonal pyramidal coordination of the Na^+ and Li^+ cations as cyan and pink polyhedra, respectively. Perovskite and intergrowth layer Pb-centered polyhedra are shaded green and yellow, respectively. Atom colors: Pb: teal; Cl: green; Na: cyan, O: red; N: blue; C: grey; Li: pink. Hydrogen and disordered atoms are omitted for clarity.

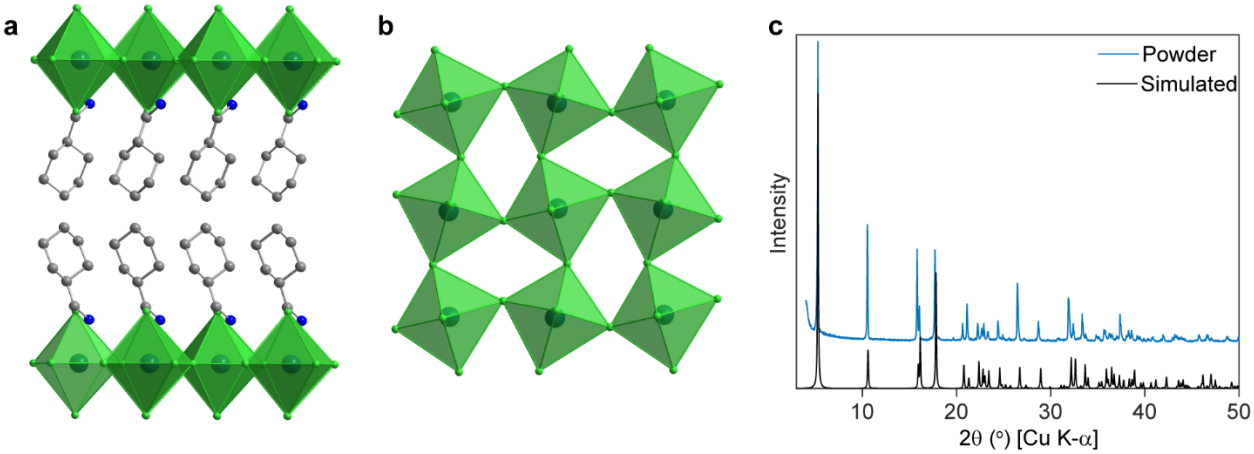

Figure S8. SC-XRD structure of the 2D perovskite $(AMC)_2PbCl_4$: a) a side view, and b) a top-down view of the inorganic layer showing the octahedral distortions. Lead-chloride polyhedra are shaded green. Atom colors: Pb: teal; Cl: green; N: blue; C: grey. Hydrogen atoms are omitted for clarity. c) Experimental (blue) and simulated (black) PXRD pattern for $(AMC)_2PbCl_4$.

Table S6. Structural distortion parameters for the perovskite and intergrowth layers of both the heterostructures compared to those of the 2D perovskite $(AMC)_2PbCl_4$. Note that D_{in} and D_{out} values are similar for the perovskite layers across the three materials (green highlighting) but different in the intergrowths of the two heterostructures.

Structure	Layer	D_{in} (°)	D_{out} (°)
$(AMC)_2PbCl_4$	Perovskite	22.6	0
1_Na	Perovskite	21.3	0
	Intergrowth	11.4	8.5
1_Li	Perovskite	22.8	0.06
	Intergrowth	0.9	6.1

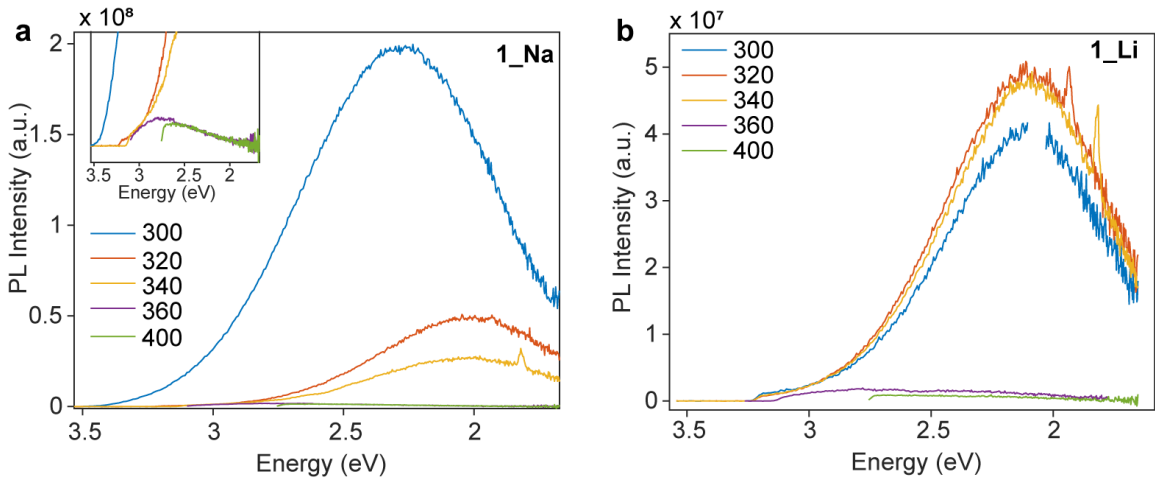

Figure S9. Room-temperature photoluminescence (PL) spectra for a) **1_Na** and b) **1_Li** with different excitation wavelengths (in nm). There is no Stokes-shifted broad emission with excitation well below the bandgap (360 and 400 nm). Inset of (a) shows enlarged PL spectra with sub-bandgap excitation showing a completely different line shape.

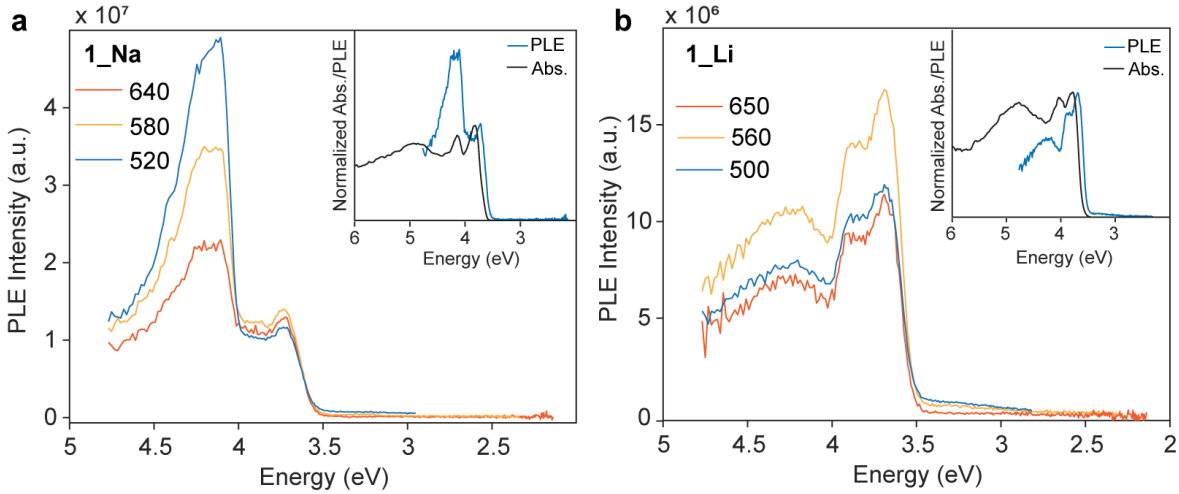

Figure S10. Room-temperature photoluminescence excitation (PLE) spectra for a) **1_Na** and b) **1_Li** probed at different emission wavelengths (in nm) across the broad emission spectra. Insets show the normalized excitation spectra (blue) overlayed with diffuse reflectance (black).

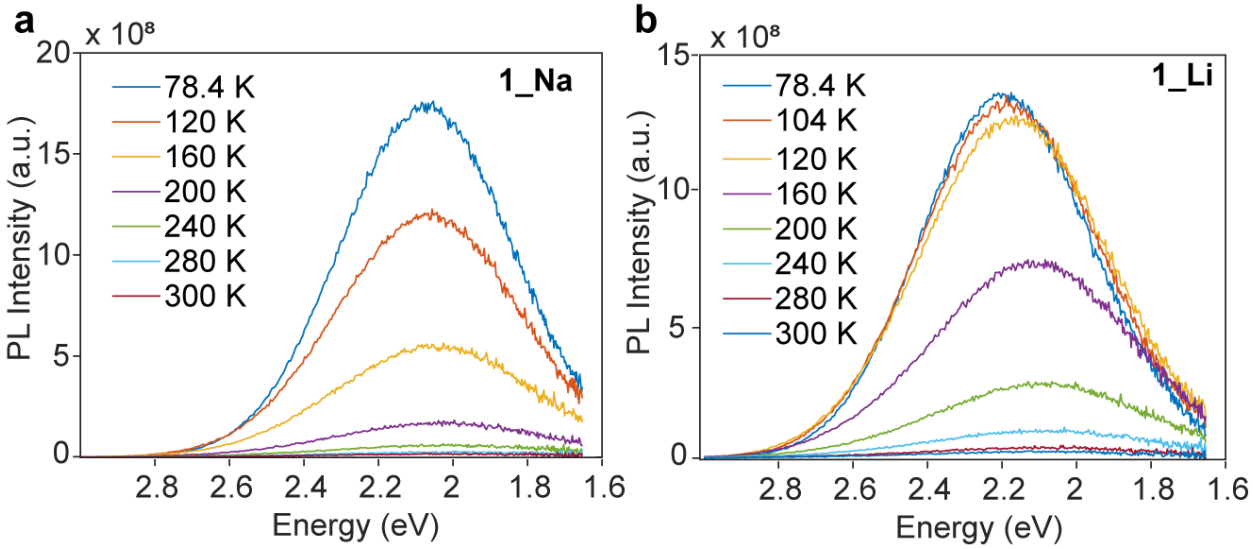

Figure S11. Temperature-dependent PL spectra of the heterostructure powders dispersed in a PMMA matrix for a) **1_Na** and b) **1_Li**.

Supplementary Note 1: Temperature-dependent FWHM and PL intensity fitting

The FWHM broadening due to exciton-phonon interactions can be modelled using eq. (S1).[17,18]

$$FWHM(T) = 2.35\sqrt{s}\,E_{ph}\sqrt{\coth\left(E_{ph}/2.k_B T\right)} \qquad \text{Equation S1}$$

where s and E_{ph} are the fitting parameters denoting the Huang-Rhys parameter and effective phonon energy, respectively, k_B is the Boltzmann constant, and T is the temperature. The fits and the fitted parameters for FWHM are shown in Figure S11 and Table S7, respectively. Although E_{ph} is quite similar for both the samples, as expected for the similar structures, **1_Na** has a much higher Huang-Rhys parameter than **1_Li** hinting at stronger exciton-phonon coupling in **1_Na**. Assuming that the temperature-dependent PL quenching is a result of a non-radiative relaxation process with an energy barrier of E_1, a sigmoidal dependence of PL intensity on temperature described by equation S2 is expected.[17,19] Temperature-dependent PL intensities were fit to the following equation:[17,19]

$$I(T) = \frac{I_0}{1 + A\,e^{\frac{-E_1}{k_B T}}} \qquad \text{Equation S2}$$

where I_0 is a constant related to the maximum intensity plateau at low temperature, A and E_1 are a constant prefactor and the activation energy for the decay process, respectively. The resulting fits are shown in Figure S12. The obtained energy barrier for **1_Li** is $E_1 = 116$ meV whereas that for **1_Na** is $E_1 = 79$ meV. The higher energy barrier of **1_Li** is evident from Figure S12 as the PL intensity plateaus at a higher temperature than **1_Na**. A full list of the fitting parameters for temperature-dependent PL intensities are shown in Table S8.

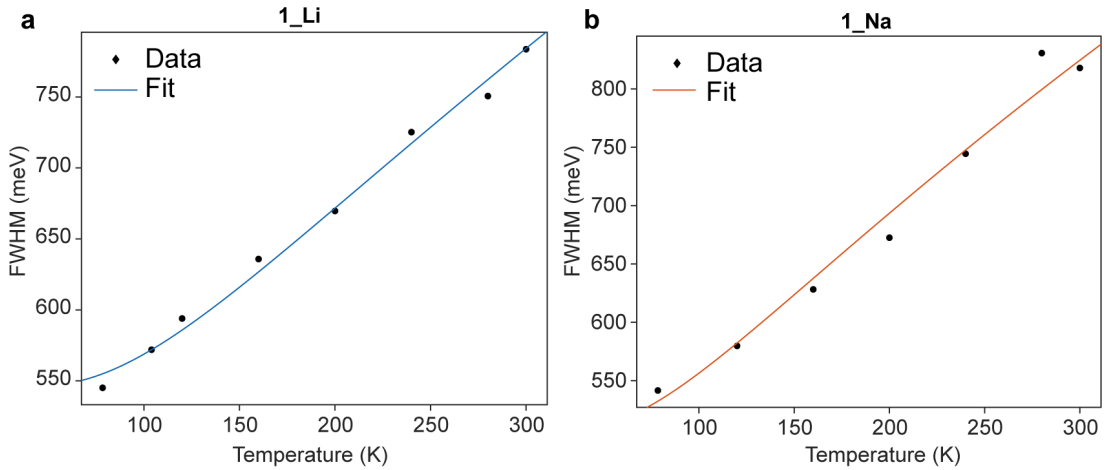

Figure S12. Temperature-dependent FWHM (circles) and the corresponding fit (solid lines) to equation S1 for a) **1_Li**, and b) **1_Na**. Fitting parameters and R^2 values are given in Table S7.

Table S7. Obtained fitting parameters and the goodness-of-fit (R^2) from temperature-dependent FWHM using equation S1.

Sample	s	E_{ph} (meV)	R^2
1_Na	108.60	20.65	0.9787
1_Li	71.75	27.28	0.9917

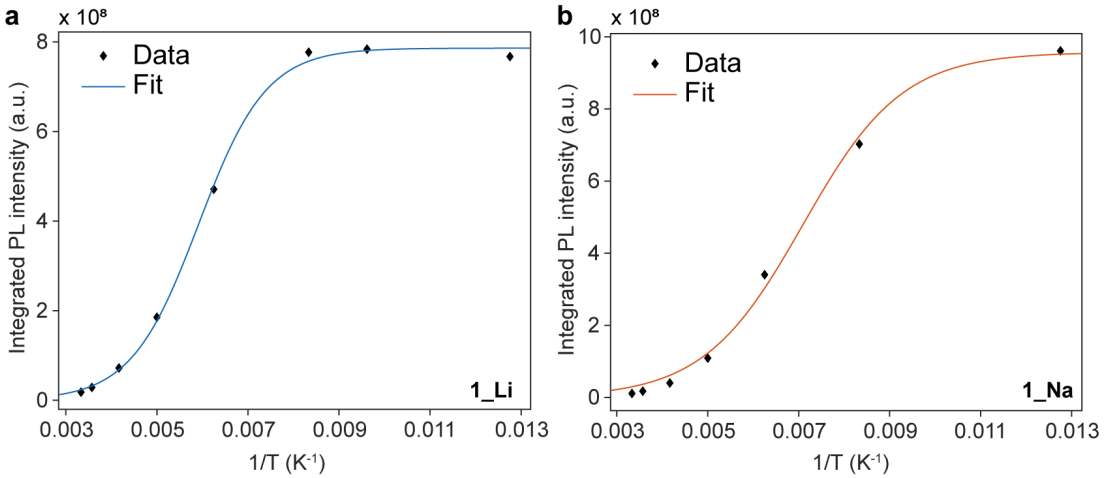

Figure S13. Temperature-dependent PL intensity (diamonds) and the corresponding fit (solid lines) to equation S2 for a) **1_Li**, and b) **1_Na**. Fitting parameters and R^2 values are given in Table S8.

Table S8. Obtained fitting parameters and the goodness-of-fit (R^2) from temperature-dependent PL intensity using equation S2.

Sample	I_0	A	E_1/k_B (K)	E_1 (meV)	R^2
1_Na	9.571×10^8	660	916	79	0.9961
1_Li	7.862×10^8	2874	1346	116	0.9989

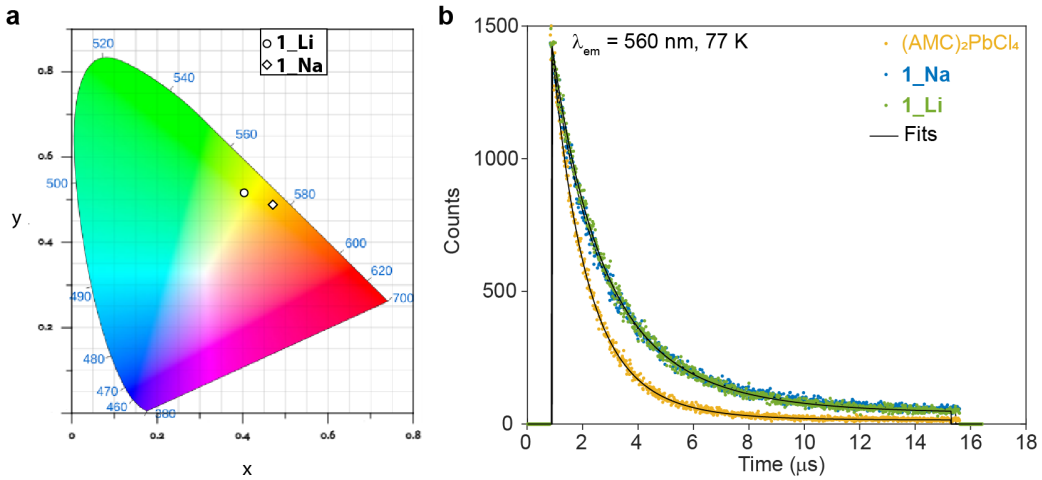

Figure S14. a) CIE 1931 coordinates for **1_Li** and **1_Na** calculated from 78-K PL spectra, and b) PL decay curves at 77 K with 331 nm excitation and 560 nm emission wavelength for the 2D perovskite $(AMC)_2PbCl_4$ (yellow), **1_Na** (blue), and **1_Li** (green) along with biexponential fits (black lines). Fit parameters are given in Table S9. The **1_Na** and **1_Li** heterostructures show very similar lifetimes.

Table S9. Fitting parameters for the PL lifetimes obtained from biexponential fits along with the χ^2 value

Sample	τ_1 **(μs)**	a_1 **(%)**	τ_2 **(μs)**	a_1 **(%)**	τ_{avg} **(μs)**	χ^2
$(AMC)_2PbCl_4$	1.06	51.67	2.08	48.33	1.55	1.1459
1_Na	1.23	25.82	3.04	74.18	2.57	1.0894
1_Li	1.50	39.65	3.26	60.35	2.56	1.0957

Table S10. Comparison of the electronic and optical bandgaps obtained from theory with the experimental optical absorption onsets (in eV).

	1_Li	**1_Na**	Value for **1_Na** – value for **1_Li**
Experiment (optical)[a]	3.78	3.83	0.05
DFT (electronic)	1.66	2.37	0.71
GW (electronic)	3.09	3.87	0.78
BSE (optical)	3.06	3.01	–0.05

[a] Values denote the lowest-energy excitonic peak positions since Tauc plot analysis is not applicable here.

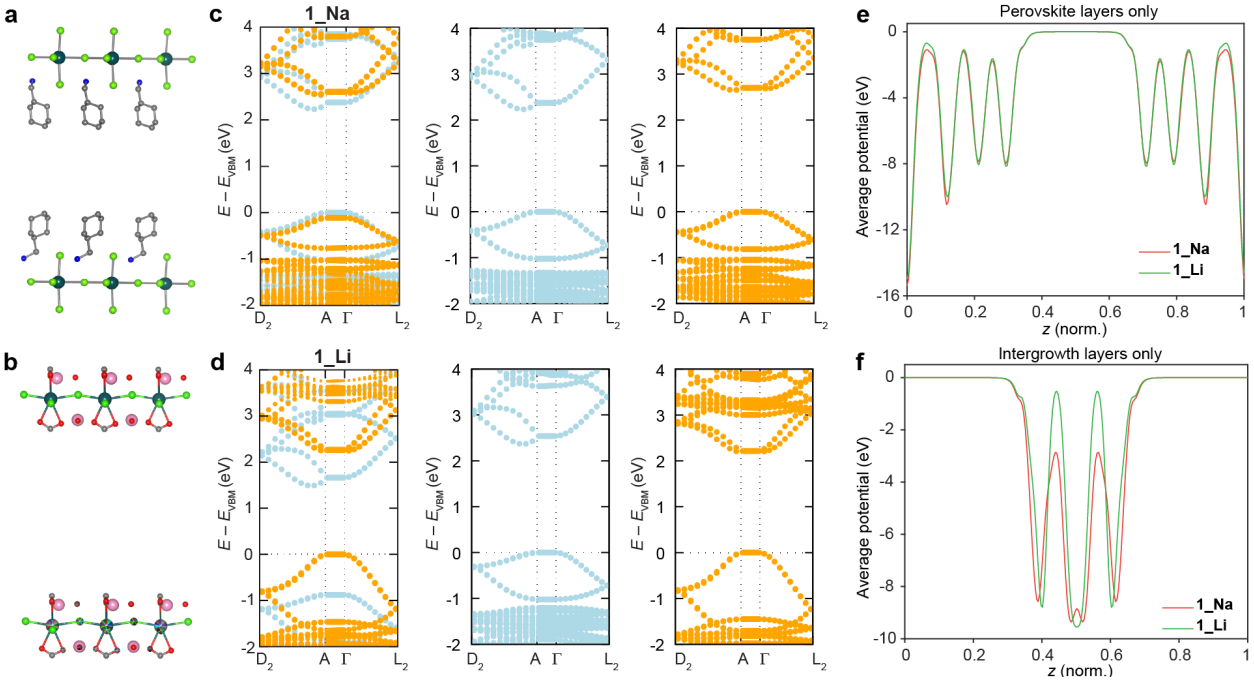

Figure S15. Model structures derived from the full heterostructure of **1_Li** where the a) perovskite and b) intergrowth layers are isolated, atom colors: Pb: teal; Cl: green; O: red; N: blue; C: grey; Li: pink. Hydrogen atoms are omitted for clarity. Band structures of the full heterostructure (left panels), of isolated perovskite layers (middle panels), and of isolated intergrowth layers (right panels) for c) **1_Na** and d) **1_Li**. Bands derived from perovskite states are shown in blue and those from intergrowth states are shown in orange. Comparison of the planar-averaged potential profiles of both the heterostructures along the interlayer direction (*z*) normalized to the unit-cell length for e) perovskite layers and f) intergrowth layers. The potential profiles are aligned to the potential energy of the region in between two neighboring layers, which we approximate to be the vacuum level. The potential profiles of the intergrowth layers show significant differences between the two heterostructures whereas those of the perovskite layers are very similar.

Supplementary Note 2: Investigation of the band alignment differences between 1_Na and 1_Li

To understand the origin of the shift from a Type-I bulk quantum-well structure in **1_Na** to a Type-II structure in **1_Li**, we performed a series of calculations with systematic modifications to the structures of **1_Na** and **1_Li**. We calculated the average potential-energy profiles $V_{bare}+V_H$ along the direction perpendicular to the inorganic layers, where V_{bare}, V_H denote the electrostatic potential originating from the ions and electronic charge density, respectively.

We compared the potential profiles of the perovskite and intergrowth parts separately, by aligning
the profiles to the potential energy of the region in between two neighboring layers. First, we separated the perovskite and intergrowth components of each heterostructure, into two bulk model structures depicted in Figure S14a-b. In the separated structures, the alkali metal cations and the carboxylate groups were kept in the intergrowth, whereas the remaining part of the organoammonium molecule was assigned to the perovskite layer. Hydrogen atoms were introduced at the positions where covalent bonds were artificially removed after separation. All other structural parameters were kept unchanged to minimize artificial effects. We computed the band structure and potential profile in each case (Figure S14c-f). We find that the valence band width of the isolated intergrowth part is slightly larger than that of the original structures. However, the band-edge dispersion and individual band gaps of the isolated substructures remain nearly unchanged compared to those of the original heterostructures.

Furthermore, the separated perovskite layers of **1_Na** and **1_Li** exhibit very similar band structures (Figure S14c-d) as expected, given the similarities in the perovskite sublattice between the two. In contrast, the separated intergrowth layers show clear differences in the bandwidth of the valence band top between **1_Na** and **1_Li**, likely arising from subtle structural distortions and rearrangements of atoms and charge densities. This suggests that any variations in the overall band alignment between **1_Na** and **1_Li** originate primarily from the alkali metal atoms or intergrowth layers.

The potential profiles of the perovskite layers from each heterostructure are shown in Figure S14e, with the two profiles aligned to the potential energy of the region in between two neighboring perovskite layers, which can be approximated as the vacuum level. We find that the potential profiles of the perovskite layers originating from **1_Na** and **1_Li** are nearly identical, consistent with the experimental observation that the perovskite layer substructures in the two cases are very similar (Table S6). Similarly, upon comparing the potential profiles of the intergrowth layers (Figure S14f), aligning to the potential energy of the region between two intergrowth layers, we found a substantial difference between the two profiles, again consistent with experimentally observed structural changes (Table S6). We quantify this difference by calculating an average potential across the unit cell in each case and tracking this value in our analysis of model structures. First, we tested whether the chemical identity of the alkali metal cation is the cause for this difference. The band structures and potential profiles of the model structures with Li^+ and Na^+ swapped within the two heterostructure frameworks are nearly identical and shown in Figures 5 and S15, respectively.

Then we investigated the effect of the position of the alkali metal cation by studying a series of hypothetical structures where Na^+ is gradually moved closer to the site occupied by Li^+ in **1_Li**, but within the framework of **1_Na**. The "Li^+" site was approximated as the closest equivalent position in **1_Na**, but it is not identical to the original site due to the differences in the two heterostructure unit cells. The band structures and potential profiles for this series of structures are shown in Figures 6 and S16a and band offset (the energy difference between the valence band maxima or the conduction band minima of the intergrowth-derived bands and the perovskite-derived bands) as a function of the volume-averaged potential across a unit cell is shown in Figure S16b. Separate structural relaxation studies (see Supplementary Note 3) further reveal that the orientation of the H_2O molecule also plays an important role in determining band alignment.

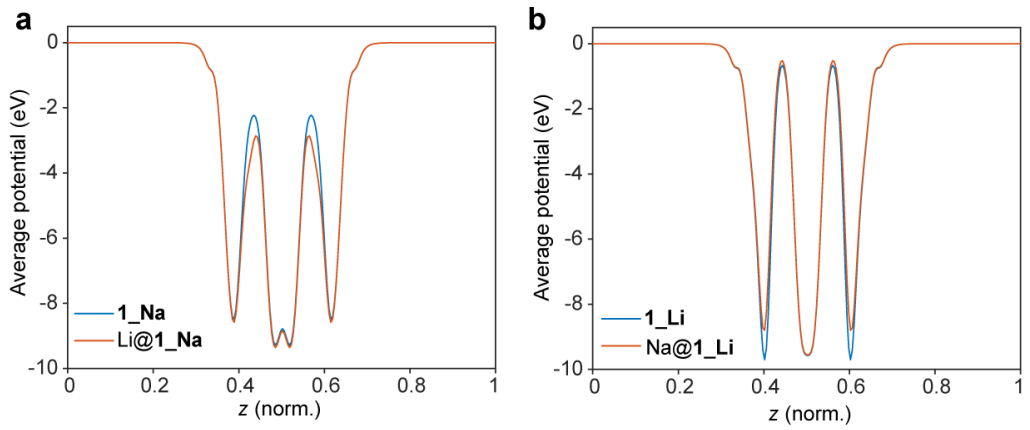

Figure S16. Planar-averaged potential profiles along the interlayer direction (*z*) normalized to the unit-cell length for a) **1_Na** and for a model structure where Na^+ is replaced with Li^+ in **1_Na** (Li@**1_Na**), and for b) **1_Li** and for a model structure where Li^+ replaced with Na^+ in **1_Li** (Na@**1_Li**). Corresponding band structures are shown in Figure 5.

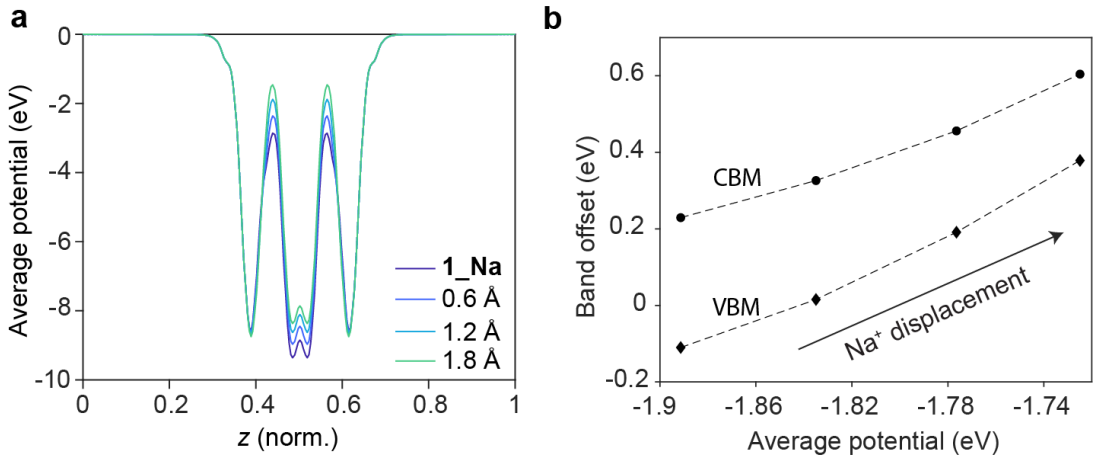

Figure S17. a) Planar-averaged potential profiles of the intergrowth layer along the interlayer direction (*z*) normalized to the unit-cell length for **1_Na** and of model heterostructures where the position of Na^+ is moved gradually towards the position of Li^+ within **1_Li** (distance shown in the legend) while keeping the rest of the framework fixed to that of **1_Na**, and b) band offsets, defined as the energy difference between the valence-band maxima (VBM; diamonds) or the conduction-band minima (CBM; circles) of the intergrowth-derived bands and the perovskite-derived bands versus the volume-averaged potential showing a

nearly linear correlation. Dashed lines are a guide to the eye. Corresponding band structures for this series are shown in Figure 6.

Supplementary Note 3: Structural Relaxations

Structural relaxations were performed using DFT with the PBE functional, with and without van der Waals corrections, using the DFT-D3 scheme of Grimme,[20] and the same computational setup as for the electronic structure calculations described above. The optimized lattice parameters and total energies per atom before and after structural relaxation are shown in Table S11. The CIFs for the final structures are provided as supplementary files.

Table S11. Lattice parameters and relative total energies per atom for experimental and DFT-optimized structures of **1_Li** and **1_Na** structures with and without van der Waals (VdW) interactions. The H_2O angle is determined from the angle between the plane of the H_2O molecule and the (002) crystallographic plane.

Structures	*a* (Å)	*b* (Å)	*c* (Å)	Volume (Å^3)	$E - E_{\text{Ref}}{}^*$ (meV/atom)	H_2O angle (º)
1_Li experiment	8.0506	7.8685	23.6145	1495.7092	0	10
1_Li relaxed w/ vdW	8.09870 (0.6%)	7.72218 (–1.9%)	23.42985 (0.8%)	1465.0466 (–2%)	–183.1475	47
1_Li relaxed w/o vdW	8.23581 (2.3%)	7.89121 (0.3%)	23.76697 (0.6%)	1544.2592 (3.2%)	–183.1087	50
1_Na experiment	8.1801	7.7431	23.3730	1479.1170	0	24
1_Na relaxed w/ vdW	8.23986 (0.7%)	7.61658 (–1.6%)	23.24279 (0.6%)	1457.1251 (–1.5%)	–320.2292	14
1_Na relaxed w/o vdW	8.38184 (2.5%)	7.74821 (0.1%)	23.58485 (0.9%)	1530.3051 (3.5%)	–320.7723	13

* Referenced to a self-consistent field calculation using DFT-PBE with van der Waals interaction on experimental structures, calculated for **1_Li** and **1_Na**, respectively

Figure S18 shows the band structures of the optimized structures of both the heterostructures, with van der Waals forces. We find that **1_Na** maintains a Type-I band alignment and **1_Li** maintains a Type-II alignment upon structural relaxation. However, the valence-band offset for **1_Li** (energy difference between the highest-filled perovskite-based band and the highest-filled intergrowth based band) is reduced to 0.15 eV (compared to the 0.88 eV offset calculated for the unrelaxed structure).

In the absence of dispersive forces (i.e., without van der Waals corrections) we find **1_Na** retains the Type-I band alignment, whereas **1_Li** converts to a Type-I band alignment with a very small valence band offset of 0.08 eV (Figure S19). The band alignment types and band edge offsets in each case are reported in Table S12.

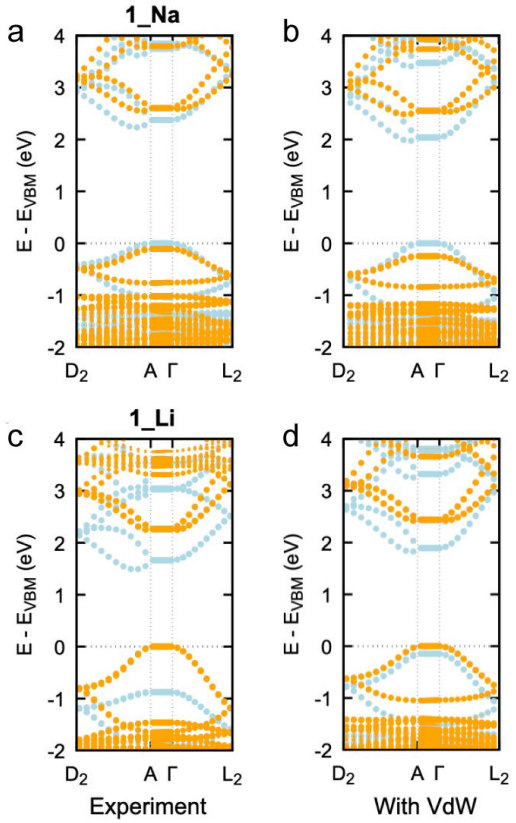

Figure S18. Band structures of a) the experimentally refined structure of **1_Na**, b) the geometry optimized structure of **1_Na** with van der Waals interactions, c) the experimentally refined structure of **1_Li** and d) the geometry optimized structure of **1_Li** with van der Waals interactions. Bands derived from perovskite states are shown in blue and those from intergrowth states are shown in orange.

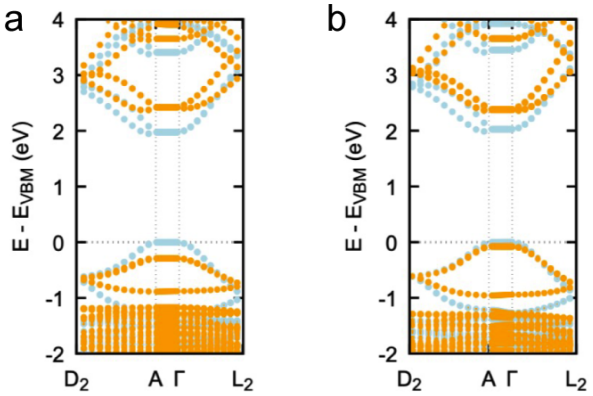

Figure S19. Band structures of the geometry optimized structures of a) **1_Na** and b) **1_Li**, both without van der Waals interactions. Bands derived from perovskite states are shown in blue and those from intergrowth states are shown in orange.

Table S12. Band offset (the energy difference between the valence band maxima or the conduction band minima of the intergrowth-derived bands and the perovskite-derived bands) for experimental and DFT-optimized structures of **1_Li** and **1_Na** structures with and without van der Waals interactions.

Structures	VBM(per.)–VBM(int.) (eV)	CBM(per.)–CBM(int.) (eV)	Alignment
1_Li experiment	–0.8768	–0.6017	Type II
1_Li relaxed w/ VdW	–0.148	–0.546	Type II
1_Li relaxed w/o VdW	0.0786	–0.3515	Type I
1_Na experiment	0.11	–0.2294	Type I
1_Na relaxed w/ VdW	0.2479	–0.5145	Type I
1_Na relaxed w/o VdW	0.2906	–0.4456	Type I

Comparison between the relaxed and experimentally refined structures reveals two major differences: (1) subtle changes in octahedral tilting and distortion in the perovskite layers, and in the

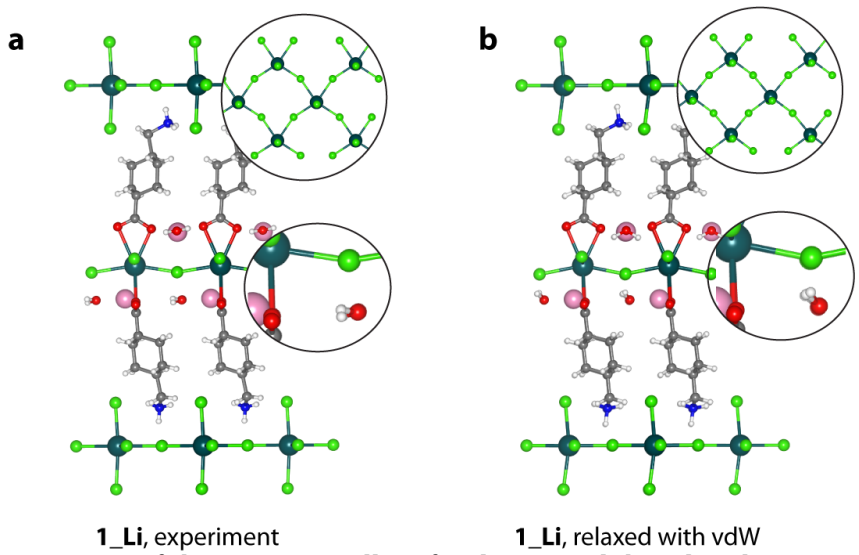

Figure S20. Structures of the experimentally refined **1_Li** and the relaxed **1_Li** with DFT-PBE with van der Waals interactions. Top insets show the top-down view of the perovskite layers. Bottom insets show the orientation of the water molecule. Atom colors: Pb: teal; Cl: green; O: red; N: blue; C: grey; Li: pink; H: white.

bandwidth of the perovskite states, and (2) reorientation of the H_2O molecules from a configuration where the plane of the molecule is roughly parallel to the plane of the inorganic sheets to a more "tilted" one (Figure S20). Since the H atoms cannot be located in the electron density maps, the SC-XRD data cannot distinguish between these two orientations, and the water molecules may be disordered between these orientations.

Since the reorientation of the H_2O molecules was the main structural difference between the experimental and geometry optimized structures of **1_Li**, we sought to isolate the impact of the water molecule re-orientation on the electronic structure. We took the **1_Li** structure obtained from structural optimization with van der Waals interactions (keeping the framework, and Li atoms frozen in place) and manually changed the orientation and position of the water molecules to match the molecules in the experimental refinement. The water molecules were thus tilted from their original positions (with the planes of the molecules at a 47° angle to the (002) crystallographic plane) to ones where the planes of the water molecules were at a 10° angle to the (002) crystallographic plane. We find that the water molecule orientation alone can significantly increase the valence band offset from approximately 150 meV to more than 1 eV, when all other structural parameters remain fixed (Figure S21).

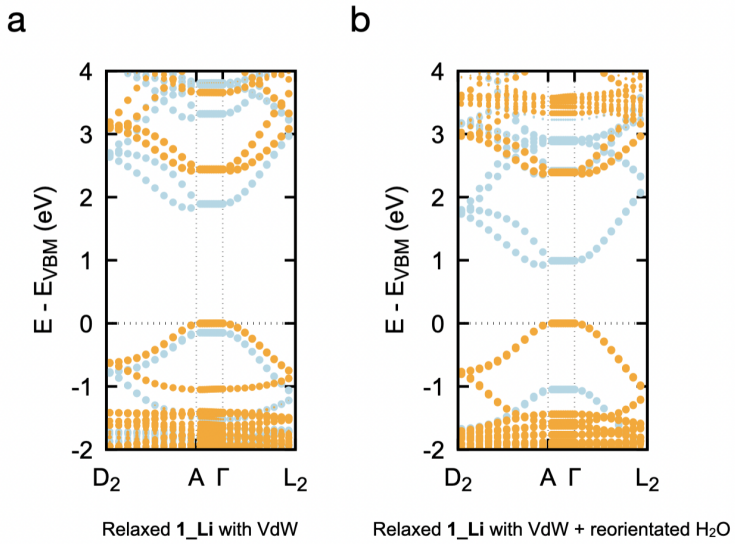

Figure S21. Electronic band structures of a) **1_Li** obtained from structural optimization with van der Waals interactions and b) the same **1_Li** structure with the planes of the water molecules manually reoriented, from an angle of 47° to an angle of 10°, with respect to the (002) crystallographic plane. This artificial structure was constructed to isolate the effects of reorienting the water molecules.

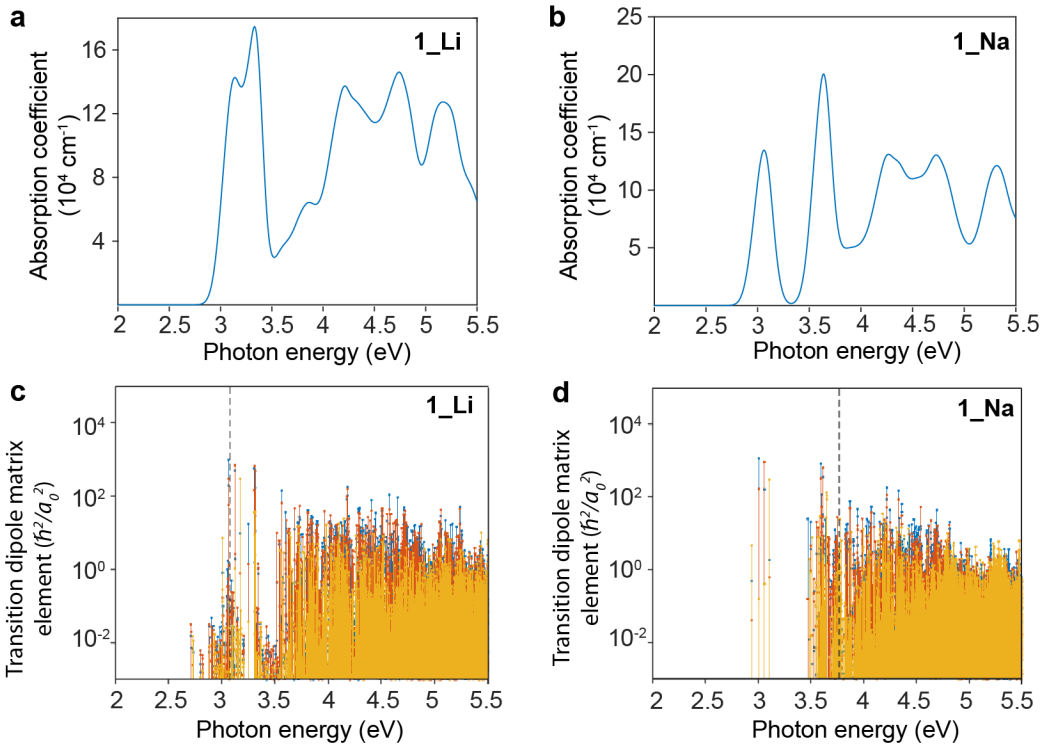

Figure S22. Calculated linear optical absorption spectra with electron-hole interactions (*GW*+BSE) for a) **1_Li** and b) **1_Na**. Calculated transition dipole matrix elements along the three directions, parallel (red, blue) and perpendicular (yellow) to the plane of the inorganic layers for c) **1_Li** and d) **1_Na**. The quasi-particle band gaps are shown in dashed black lines. The lowest-energy transition for **1_Li** has a low oscillator strength, making it optically dark whereas the lowest-energy transition for **1_Na** is bright. Two bright excitonic states, corresponding to the peaks in the absorption spectra, are seen in both **1_Li** and **1_Na**.

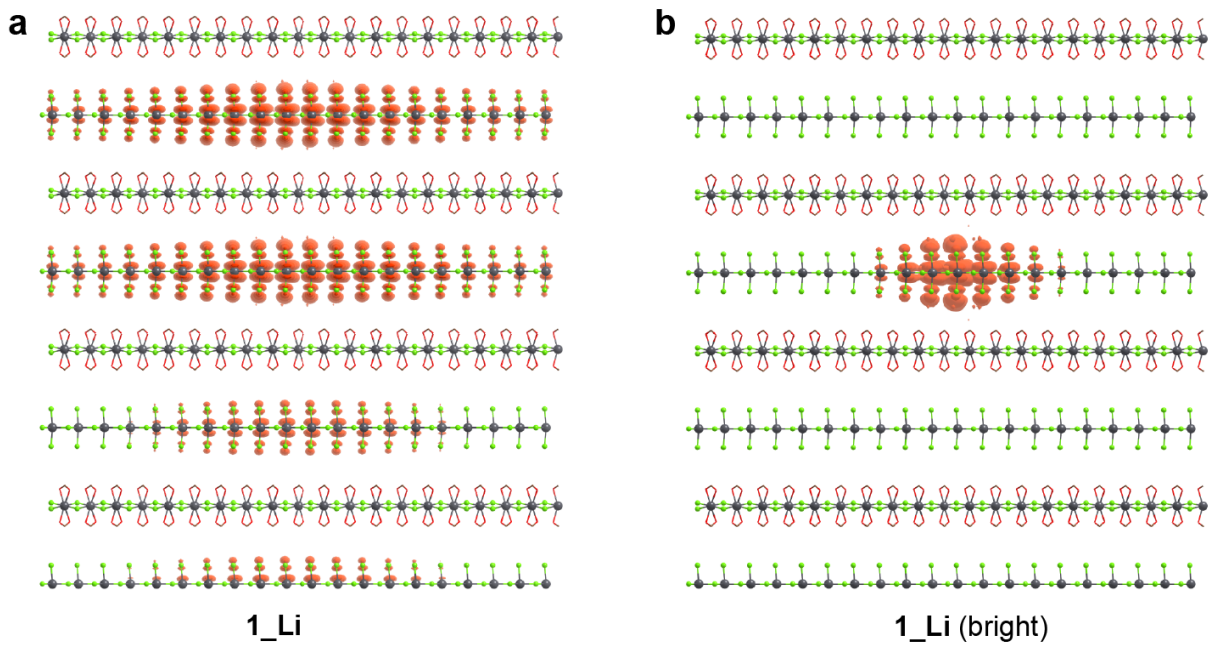

Figure S23. Isosurfaces representing the spatial distribution of the photoexcited electron corresponding to a) the lowest energy (dark) exciton state in **1_Li**, when the hole position is fixed to the center of an inter-growth layer (showing the extended supercell from Figure 8C) and b) the lowest-energy bright exciton state in **1_Li**, when the hole position is fixed to the center of a perovskite layer. Pb and Cl atoms are represented by gray and green spheres, respectively. The carboxylate group is denoted by red sticks; the rest of the ligands, water molecules, and alkali metal cations are omitted for clarity.

Table S13. The SHG power law obtained by fitting the power dependence data to $y = a\,x^{b}$ and goodness-of-fit (R^2) values.

Sample	Power (b)	R^2
1_Li	2.05	0.9999
1_Na	2.12	0.9998
Quartz	1.97	0.9991

Supplementary Note 4: Calculation of effective second order susceptibility coefficient (d_{eff})

To assess the strength of the optical nonlinearity for SHG, we performed SHG measurements in reflection mode on the heterostructures and compared this signal to that from a 1 mm thick piece of Z-cut quartz. The reflected second-harmonic signal is propagating in the completely non-phase

matched direction, with a coherence length scaling as $[2k_{\omega}+k_{2\omega}]^{-1}$, where k_{ω} and $k_{2\omega}$denote the wavevectors in the material at the fundamental and second harmonic wavelengths, respectively.[21] Thus, the conversion efficiency will be low and pump depletion can be neglected. In contrast to a nearly phase-matched situation, the conversion efficiency will also have a relatively weak dependence on the refractive index and its dispersion. Therefore, for estimating the nonlinearity of the samples, we neglect the difference between the coherence lengths of the samples and the quartz reference, which is modest since the refractive indices are fairly similar (~1.8 for Pb–Cl perovskites based on previous experiments[22,23] and 1.544 for quartz as specified by the manufacturer). Likewise, we neglect the difference in the Fresnel factors for the beam entering and leaving the sample and reference. Using the scaling between fundamental and second-harmonic electric fields and an effective thickness given by the coherence length, we can then write the following eqation.[21]

$$\left|\frac{d_{eff}^{p}}{d_{eff}^{q}}\right| = \sqrt{\frac{I_{2\omega}^{p}}{I_{2\omega}^{q}}} \cdot \frac{I_{\omega}^{q}}{I_{\omega}^{p}} \cdot \frac{L^{q}}{L^{p}} \qquad \text{Equation S3}$$

Here, I, and L refer to the intensity and effective thickness, respectively. Superscripts p and q denote the perovskite heterostructure sample and quartz references, respectively. Subscripts ω and 2ω refer to the fundamental and second harmonic frequencies, respectively. We assume that the beam profile and pulse duration are the same in the two cases, as is realized experimentally. For the quartz reference, the value of d_{eff} is taken from the literature ($d_{11} = 0.30$ pm/V).[24] Substituting in equation S3, we obtain $d_{eff} = 11.2$ pm/V for **1_Na** (~37 × quartz) and $d_{eff} = 14.9$ pm/V for **1_Li** (~50 × quartz). We note that the inclusion of the larger index of refraction for the sample compared with the quartz reference in our estimate would slightly increase the inferred nonlinearity of the sample, since the left-hand side of Equation S3 is directly proportional to the ratio of the refractive indices of the sample to the reference.[21] In this analysis, we neglect possible influence of the reflection from the substrate of the forward propagating second-harmonic beam created in the perovskite sample or the quartz reference, since this light is not effectively collected in our experimental arrangement utilizing a pump beam tightly focused at the surface.

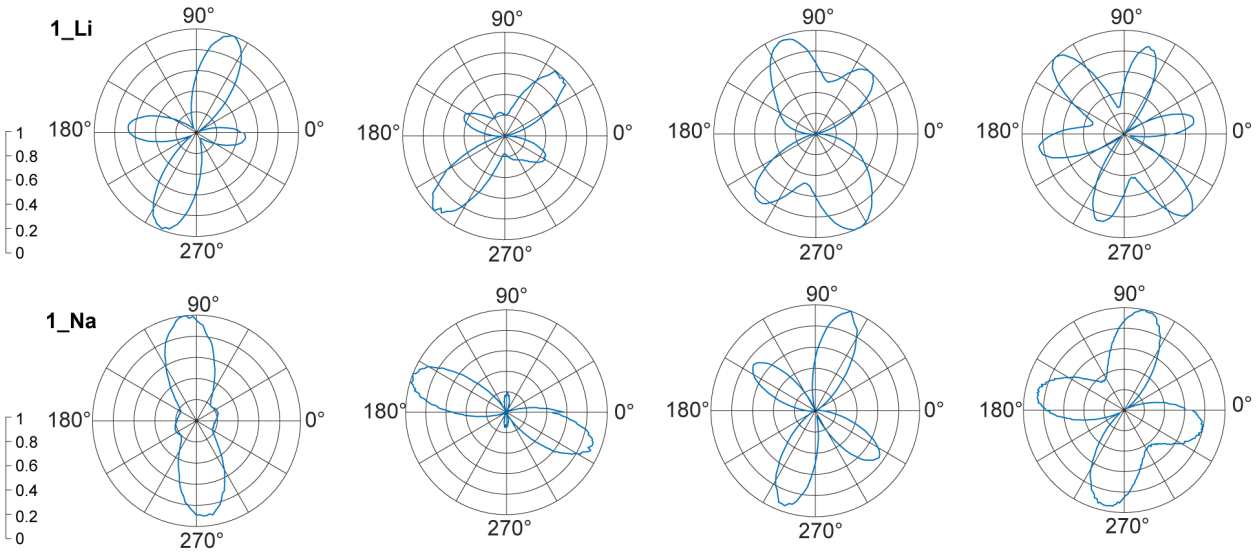

Figure S24. Representative polarization dependent SHG plots (normalized) across 3-4 crystals of **1_Li** (top row) and **1_Na** (bottom row). Each plot corresponds to a different spot. We observe 2-lobe, 4-lobe (separate or butterfly) or 6-lobe polarization patterns across the large dataset. Laser spot size ~3 m; $\lambda_{\omega} = 1030$ nm.

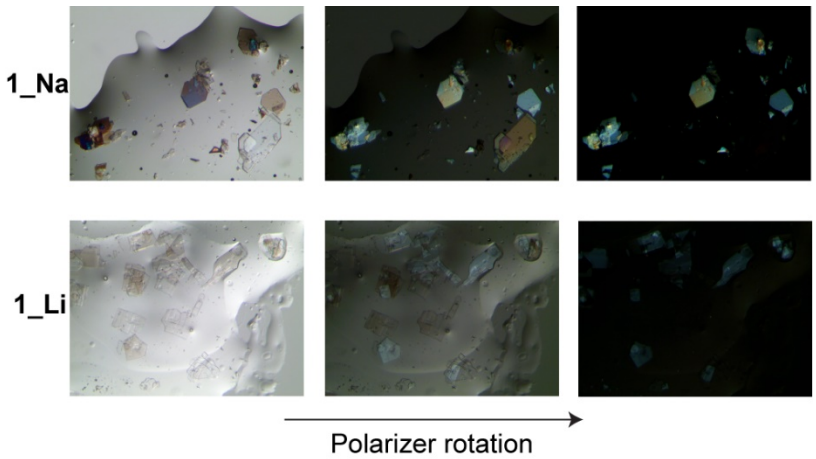

Figure S25. Images of the crystals of **1_Na** (top row) and **1_Li** (bottom row) taken from an optical microscope with different polarizer angles showing a color change with the polarization.

References

(1) Smith, M. D.; Jaffe, A.; Dohner, E. R.; Lindenberg, A. M.; Karunadasa, H. I. Structural Origins of Broadband Emission from Layered Pb–Br Hybrid Perovskites. *Chem. Sci.* **2017**, *8* (6), 4497–4504. https://doi.org/10.1039/C7SC01590A.

(2) Landi, S.; Segundo, I. R.; Freitas, E.; Vasilevskiy, M.; Carneiro, J.; Tavares, C. J. Use and Misuse of the Kubelka-Munk Function to Obtain the Band Gap Energy from Diffuse Reflectance Measurements. *Solid State Commun.* **2022**, *341*. https://doi.org/10.1016/j.ssc.2021.114573.

(3) Get the Basics Right: Jacobian Conversion of Wavelength and Energy Scales for Quantitative Analysis of Emission Spectra. **2013**, *3318* (2), 3316–3318.

(4) Hohenberg, P.; Kohn, W. Inhomogeneous Electron Gas. *Phys. Rev.* **1964**, *136* (3B), B864–B871. https://doi.org/10.1103/PhysRev.136.B864.

(5) Garrity, K. F.; Bennett, J. W.; Rabe, K. M.; Vanderbilt, D. Pseudopotentials for High-Throughput DFT Calculations. *Comput. Mater. Sci.* **2014**, *81*, 446–452. https://doi.org/10.1016/j.commatsci.2013.08.053.

(6) Giannozzi, P.; Andreussi, O.; Brumme, T.; Bunau, O.; Buongiorno Nardelli, M.; Calandra, M.; Car, R.; Cavazzoni, C.; Ceresoli, D.; Cococcioni, M.; Colonna, N.; Carnimeo, I.; Dal Corso, A.; de Gironcoli, S.; Delugas, P.; DiStasio, R. A.; Ferretti, A.; Floris, A.; Fratesi, G.; Fugallo, G.; Gebauer, R.; Gerstmann, U.; Giustino, F.; Gorni, T.; Jia, J.; Kawamura, M.; Ko, H.-Y.; Kokalj, A.; Küçükbenli, E.; Lazzeri, M.; Marsili, M.; Marzari, N.; Mauri, F.; Nguyen, N. L.; Nguyen, H.-V.; Otero-de-la-Roza, A.; Paulatto, L.; Poncé, S.; Rocca, D.; Sabatini, R.; Santra, B.; Schlipf, M.; Seitsonen, A. P.; Smogunov, A.; Timrov, I.; Thonhauser, T.; Umari, P.; Vast, N.; Wu, X.; Baroni, S. Advanced Capabilities for Materials Modelling with Quantum ESPRESSO. *J. Phys. Condens. Matter* **2017**, *29* (46), 465901. https://doi.org/10.1088/1361-648X/aa8f79.

(7) van Setten, M. J.; Giantomassi, M.; Bousquet, E.; Verstraete, M. J.; Hamann, D. R.; Gonze, X.; Rignanese, G.-M. The PseudoDojo: Training and Grading a 85 Element Optimized Norm-Conserving Pseudopotential Table. *Comput. Phys. Commun.* **2018**, *226*, 39–54. https://doi.org/10.1016/j.cpc.2018.01.012.

(8) Hamann, D. R. Optimized Norm-Conserving Vanderbilt Pseudopotentials. *Phys. Rev. B* **2013**, *88* (8), 085117. https://doi.org/10.1103/PhysRevB.88.085117.

(9) Hybertsen, M. S.; Louie, S. G. Electron Correlation in Semiconductors and Insulators: Band Gaps and Quasiparticle Energies. *Phys. Rev. B* **1986**, *34* (8), 5390–5413. https://doi.org/10.1103/PhysRevB.34.5390.

(10) Deslippe, J.; Samsonidze, G.; Strubbe, D. A.; Jain, M.; Cohen, M. L.; Louie, S. G. BerkeleyGW: A Massively Parallel Computer Package for the Calculation of the Quasiparticle and Optical Properties of Materials and Nanostructures. *Comput. Phys. Commun.* **2012**, *183* (6), 1269–1289. https://doi.org/10.1016/j.cpc.2011.12.006.

(11) Godby, R. W.; Needs, R. J. Metal-Insulator Transition in Kohn-Sham Theory and Quasiparticle Theory. *Phys. Rev. Lett.* **1989**, *62* (10), 1169–1172. https://doi.org/10.1103/PhysRevLett.62.1169.

(12) Aubrey, M. L.; Saldivar Valdes, A.; Filip, M. R.; Connor, B. A.; Lindquist, K. P.; Neaton, J. B.; Karunadasa, H. I. Directed Assembly of Layered Perovskite Heterostructures as Single Crystals. *Nature* **2021**, *597* (7876), 355–359. https://doi.org/10.1038/s41586-021-03810-x.

(13) Rohlfing, M.; Louie, S. G. Electron-Hole Excitations in Semiconductors and Insulators. *Phys. Rev. Lett.* **1998**, *81* (11), 2312–2315. https://doi.org/10.1103/PhysRevLett.81.2312.
(14) Rohlfing, M.; Louie, S. G. Electron-Hole Excitations and Optical Spectra from First Principles. *Phys. Rev. B* **2000**, *62* (8), 4927–4944. https://doi.org/10.1103/PhysRevB.62.4927.
(15) Sharifzadeh, S.; Darancet, P.; Kronik, L.; Neaton, J. B. Low-Energy Charge-Transfer Excitons in Organic Solids from First-Principles: The Case of Pentacene. *J. Phys. Chem. Lett.* **2013**, *4* (13), 2197–2201. https://doi.org/10.1021/jz401069f.
(16) Spatial Tessellations: Concepts and Applications of Voronoi Diagrams, 2nd Edition | Wiley. https://www.wiley.com/en-us/Spatial+Tessellations%3A+Concepts+and+Applications+of+Voronoi+Diagrams%2C+2nd+Edition-p-9780471986355 (accessed 2025-04-17).
(17) Mccall, K. M.; Stoumpos, C. C.; Kostina, S. S.; Kanatzidis, M. G.; Wessels, B. W. Strong Electron − Phonon Coupling and Self-Trapped Excitons in the Defect Halide Perovskites $A_3M_2I_9$ (A = Cs, Rb; M = Bi, Sb). *Chem. Mater.* **2017**, *9* (29), 2149–4145. https://doi.org/10.1021/acs.chemmater.7b01184.
(18) Li, J.; Wang, H.; Li, D. Self-Trapped Excitons in Two-Dimensional Perovskites. *Frontiers of Optoelectronics*. 2020, pp 225–234. https://doi.org/10.1007/s12200-020-1051-x.
(19) Woo, H. C.; Choi, J. W.; Shin, J.; Chin, S.; Ann, M. H.; Lee, C. Temperature-Dependent Photoluminescence of $CH_3NH_3PbBr_3$ Perovskite Quantum Dots and Bulk Counterparts. **2018**. https://doi.org/10.1021/acs.jpclett.8b01593.
(20) Grimme, S.; Antony, J.; Ehrlich, S.; Krieg, H. A Consistent and Accurate Ab Initio Parametrization of Density Functional Dispersion Correction (DFT-D) for the 94 Elements H-Pu. *J. Chem. Phys.* **2010**, *132* (15), 154104. https://doi.org/10.1063/1.3382344.
(21) Shen, Y. R. *The Principles of Nonlinear Optics | Wiley*.
(22) He, C.; Zha, G.; Deng, C.; An, Y.; Mao, R.; Liu, Y.; Lu, Y.; Chen, Z. Refractive Index Dispersion of Organic–Inorganic Hybrid Halide Perovskite $CH_3NH_3PbX_3$ (X═Cl, Br, I) Single Crystals. *Cryst. Res. Technol.* **2019**, *54* (5), 1900011. https://doi.org/10.1002/crat.201900011.
(23) Song, B.; Hou, J.; Wang, H.; Sidhik, S.; Miao, J.; Gu, H.; Zhang, H.; Liu, S.; Fakhraai, Z.; Even, J.; Blancon, J.-C.; Mohite, A. D.; Jariwala, D. Determination of Dielectric Functions and Exciton Oscillator Strength of Two-Dimensional Hybrid Perovskites. *ACS Mater. Lett.* **2021**, *3* (1), 148–159. https://doi.org/10.1021/acsmaterialslett.0c00505.
(24) Hagimoto, K.; Mito, A. Determination of the Second-Order Susceptibility of Ammonium Dihydrogen Phosphate and α-Quartz at 633 and 1064 nm. *Appl. Opt.* **1995**, *34* (36), 8276–8282. https://doi.org/10.1364/AO.34.008276.
(1) Smith, M. D.; Jaffe, A.; Dohner, E. R.; Lindenberg, A. M.; Karunadasa, H. I. Structural Origins of Broadband Emission from Layered Pb–Br Hybrid Perovskites. *Chem. Sci.* **2017**, *8* (6), 4497–4504. https://doi.org/10.1039/C7SC01590A.
(2) Landi, S.; Segundo, I. R.; Freitas, E.; Vasilevskiy, M.; Carneiro, J.; Tavares, C. J. Use and Misuse of the Kubelka-Munk Function to Obtain the Band Gap Energy from Diffuse Reflectance Measurements. *Solid State Commun.* **2022**, *341*. https://doi.org/10.1016/j.ssc.2021.114573.
(3) Get the Basics Right: Jacobian Conversion of Wavelength and Energy Scales for Quantitative Analysis of Emission Spectra. **2013**, *3318* (2), 3316–3318.
(4) Hohenberg, P.; Kohn, W. Inhomogeneous Electron Gas. *Phys. Rev.* **1964**, *136* (3B), B864–B871. https://doi.org/10.1103/PhysRev.136.B864.

(5) Garrity, K. F.; Bennett, J. W.; Rabe, K. M.; Vanderbilt, D. Pseudopotentials for High-Throughput DFT Calculations. *Comput. Mater. Sci.* **2014**, *81*, 446–452. https://doi.org/10.1016/j.commatsci.2013.08.053.
(6) Giannozzi, P.; Andreussi, O.; Brumme, T.; Bunau, O.; Buongiorno Nardelli, M.; Calandra, M.; Car, R.; Cavazzoni, C.; Ceresoli, D.; Cococcioni, M.; Colonna, N.; Carnimeo, I.; Dal Corso, A.; de Gironcoli, S.; Delugas, P.; DiStasio, R. A.; Ferretti, A.; Floris, A.; Fratesi, G.; Fugallo, G.; Gebauer, R.; Gerstmann, U.; Giustino, F.; Gorni, T.; Jia, J.; Kawamura, M.; Ko, H.-Y.; Kokalj, A.; Küçükbenli, E.; Lazzeri, M.; Marsili, M.; Marzari, N.; Mauri, F.; Nguyen, N. L.; Nguyen, H.-V.; Otero-de-la-Roza, A.; Paulatto, L.; Poncé, S.; Rocca, D.; Sabatini, R.; Santra, B.; Schlipf, M.; Seitsonen, A. P.; Smogunov, A.; Timrov, I.; Thonhauser, T.; Umari, P.; Vast, N.; Wu, X.; Baroni, S. Advanced Capabilities for Materials Modelling with Quantum ESPRESSO. *J. Phys. Condens. Matter* **2017**, *29* (46), 465901. https://doi.org/10.1088/1361-648X/aa8f79.
(7) van Setten, M. J.; Giantomassi, M.; Bousquet, E.; Verstraete, M. J.; Hamann, D. R.; Gonze, X.; Rignanese, G.-M. The PseudoDojo: Training and Grading a 85 Element Optimized Norm-Conserving Pseudopotential Table. *Comput. Phys. Commun.* **2018**, *226*, 39–54. https://doi.org/10.1016/j.cpc.2018.01.012.
(8) Hamann, D. R. Optimized Norm-Conserving Vanderbilt Pseudopotentials. *Phys. Rev. B* **2013**, *88* (8), 085117. https://doi.org/10.1103/PhysRevB.88.085117.
(9) Hybertsen, M. S.; Louie, S. G. Electron Correlation in Semiconductors and Insulators: Band Gaps and Quasiparticle Energies. *Phys. Rev. B* **1986**, *34* (8), 5390–5413. https://doi.org/10.1103/PhysRevB.34.5390.
(10) Deslippe, J.; Samsonidze, G.; Strubbe, D. A.; Jain, M.; Cohen, M. L.; Louie, S. G. BerkeleyGW: A Massively Parallel Computer Package for the Calculation of the Quasiparticle and Optical Properties of Materials and Nanostructures. *Comput. Phys. Commun.* **2012**, *183* (6), 1269–1289. https://doi.org/10.1016/j.cpc.2011.12.006.
(11) Godby, R. W.; Needs, R. J. Metal-Insulator Transition in Kohn-Sham Theory and Quasiparticle Theory. *Phys. Rev. Lett.* **1989**, *62* (10), 1169–1172. https://doi.org/10.1103/PhysRevLett.62.1169.
(12) Aubrey, M. L.; Saldivar Valdes, A.; Filip, M. R.; Connor, B. A.; Lindquist, K. P.; Neaton, J. B.; Karunadasa, H. I. Directed Assembly of Layered Perovskite Heterostructures as Single Crystals. *Nature* **2021**, *597* (7876), 355–359. https://doi.org/10.1038/s41586-021-03810-x.
(13) Rohlfing, M.; Louie, S. G. Electron-Hole Excitations in Semiconductors and Insulators. *Phys. Rev. Lett.* **1998**, *81* (11), 2312–2315. https://doi.org/10.1103/PhysRevLett.81.2312.
(14) Rohlfing, M.; Louie, S. G. Electron-Hole Excitations and Optical Spectra from First Principles. *Phys. Rev. B* **2000**, *62* (8), 4927–4944. https://doi.org/10.1103/PhysRevB.62.4927.
(15) Sharifzadeh, S.; Darancet, P.; Kronik, L.; Neaton, J. B. Low-Energy Charge-Transfer Excitons in Organic Solids from First-Principles: The Case of Pentacene. *J. Phys. Chem. Lett.* **2013**, *4* (13), 2197–2201. https://doi.org/10.1021/jz401069f.
(16) Spatial Tessellations: Concepts and Applications of Voronoi Diagrams, 2nd Edition | Wiley. https://www.wiley.com/en-us/Spatial+Tessellations%3A+Concepts+and+Applications+of+Voronoi+Diagrams%2C+2nd+Edition-p-9780471986355 (accessed 2025-04-17).
(17) Mccall, K. M.; Stoumpos, C. C.; Kostina, S. S.; Kanatzidis, M. G.; Wessels, B. W. Strong Electron − Phonon Coupling and Self-Trapped Excitons in the Defect Halide Perovskites $A_3M_2I_9$ (A = Cs, Rb; M = Bi, Sb). *Chem. Mater.* **2017**, *9* (29), 2149–4145. https://doi.org/10.1021/acs.chemmater.7b01184.
(18) Li, J.; Wang, H.; Li, D. Self-Trapped Excitons in Two-Dimensional Perovskites. *Frontiers of Optoelectronics*. 2020, pp 225–234. https://doi.org/10.1007/s12200-020-1051-x.
(19) Woo, H. C.; Choi, J. W.; Shin, J.; Chin, S.; Ann, M. H.; Lee, C. Temperature-Dependent Photoluminescence of $CH_3NH_3PbBr_3$ Perovskite Quantum Dots and Bulk Counterparts. **2018**. https://doi.org/10.1021/acs.jpclett.8b01593.
(20) Shen, Y. R. *The Principles of Nonlinear Optics | Wiley*.

(21) He, C.; Zha, G.; Deng, C.; An, Y.; Mao, R.; Liu, Y.; Lu, Y.; Chen, Z. Refractive Index Dispersion of Organic–Inorganic Hybrid Halide Perovskite $CH_3NH_3PbX_3$ (X═Cl, Br, I) Single Crystals. *Cryst. Res. Technol.* **2019**, *54* (5), 1900011. https://doi.org/10.1002/crat.201900011.
(22) Song, B.; Hou, J.; Wang, H.; Sidhik, S.; Miao, J.; Gu, H.; Zhang, H.; Liu, S.; Fakhraai, Z.; Even, J.; Blancon, J.-C.; Mohite, A. D.; Jariwala, D. Determination of Dielectric Functions and Exciton Oscillator Strength of Two-Dimensional Hybrid Perovskites. *ACS Mater. Lett.* **2021**, *3* (1), 148–159. https://doi.org/10.1021/acsmaterialslett.0c00505.
(23) Hagimoto, K.; Mito, A. Determination of the Second-Order Susceptibility of Ammonium Dihydrogen Phosphate and α-Quartz at 633 and 1064 Nm. *Appl. Opt.* **1995**, *34* (36), 8276–8282. https://doi.org/10.1364/AO.34.008276.